

Chapter 4

Swift-Hohenberg model for tilted magnetic fields

4.1 Introduction

The weakly nonlinear models discussed in the previous chapter used ideas from equivariant bifurcation theory to determine the patterns that might be observed in various circumstances. The main assumption made was that the patterns were to be doubly periodic with respect to some lattice (either rhombic or hexagonal), which led to a small number of ODEs describing the dynamics. We now wish to extend the model to allow ϕ (the angle of tilt of the magnetic field) to vary with position, as a simple way of modelling solar pores and sunspots, where the magnetic field fans out and becomes more inclined as one moves radially outwards.

Our approach will be to start from the Swift-Hohenberg equation (Swift and Hohenberg, 1977), a commonly used model equation for convection problems, in which the full three-dimensional governing equations are reduced to a single PDE in two spatial dimensions. This is a useful model since it exhibits many of the properties of convection, at least in the weakly nonlinear regime, but it is much simpler to work with than the full equations. We will add some extra terms to the usual Swift-Hohenberg equation, in order to represent the effects of the tilted magnetic field. These terms will be discussed in section 4.2.

Before studying this modified Swift-Hohenberg equation in its own right, we will first use it to derive a set of three Landau-Ginzburg equations. This represents a further simplification, since it converts the problem from a PDE in two spatial dimensions to a

system in one spatial dimension. This makes it easier to understand what is happening, albeit with some loss of generality. These equations will be derived in section 4.3.

We then move on, in section 4.4, to look at the properties of the modified Swift-Hohenberg equation itself. Using the Swift-Hohenberg equation allows us to look at more general situations, and one of the things we will do is to adapt the equation to a circular (rather than Cartesian) geometry, in order to represent a sunspot slightly more realistically. Finally, we present our conclusions in section 4.5.

4.2 The model

We consider the following modification of the Swift-Hohenberg equation:

$$\frac{\partial \psi}{\partial t} = r\psi - (1 + \nabla^2)^2 \psi + \alpha \psi^2 - \gamma \psi^3 + a\phi^2 \psi + b\phi^2 \frac{\partial^2 \psi}{\partial x^2} + c\phi \frac{\partial \psi}{\partial x}, \quad (4.1)$$

where $\psi = \psi(x, y, t)$ and $\phi = \phi(x)$ are real functions, and r, a, b, c, α and γ are real constants. When $\phi = 0$ we recover the original Swift-Hohenberg equation (with added quadratic term). The last three terms on the right-hand side are new and represent the effects of the tilted field (under the assumption that ϕ is small).

The effects of these new terms are best seen by looking at the linearized version of (4.1). If ϕ is constant we can look at the linear theory very easily, substituting $\psi = \exp(i\mathbf{k} \cdot \mathbf{x} + \sigma t)$ (with $\mathbf{k} = (k_x, k_y)$). The following equation for σ is obtained:

$$\sigma = (r + a\phi^2) - (1 - |\mathbf{k}|^2) - bk_x^2 \phi^2 + ik_x c\phi. \quad (4.2)$$

We can now see that the term proportional to a simply causes the growth rate to increase in proportion to ϕ^2 . This represents the fact that as the field tilt increases (at fixed total field strength), the critical Rayleigh number falls, and the convection becomes more vigorous (at fixed Rayleigh number).

The term proportional to b introduces a (linear) anisotropy, so that the linear growth rate of a mode depends on its orientation. Modes with $k_x \neq 0$ are penalized, so that the most unstable mode has $\mathbf{k} = (0, 1)$, corresponding to rolls aligned with the tilt direction of the magnetic field.

The term proportional to c models the fact that patterns travel when ϕ is non-zero. If ϕ was uniform, this term could be removed by transforming to an appropriate moving frame, but when ϕ depends on position, it must be retained.

Note that symmetry considerations imply that the travelling term is an odd function of ϕ , and therefore proportional to ϕ (for small ϕ), while the other two new terms are even in ϕ , and therefore proportional to ϕ^2 at leading order.

Modifications of the Swift-Hohenberg equation, including anisotropy, have been studied before. These can be divided into two classes: those in which the quadratic term (representing broken up-down symmetry) is included, and those in which it is not. An example of the latter is the work of Pesch and Kramer (1986), who applied a modified Swift-Hohenberg equation to anisotropic liquid crystal systems. Another example is in the field of rotating convection, where Roxin and Riecke (2002, 2004) apply an anisotropic Swift-Hohenberg model. A more detailed model of anisotropic rotating convection (with mean flows included) is given by Pollicott et al. (2003).

Examples of models including both anisotropy effects and the quadratic term are given by Walgraef and Schiller (1987) and Schmitz and Zimmermann (1997). Here, a transition from hexagons to rolls is found as the anisotropy increases (as in our model). However, the ‘travelling’ term (proportional to c) has not been included in any previous studies, and this term creates interesting new effects, as we shall see below.

4.3 Landau-Ginzburg equations

From the above model it is possible to derive a set of amplitude equations of Landau-Ginzburg type. We introduce a small parameter ϵ and make the following transformations:

$$r = \epsilon^2 r_2 \tag{4.3}$$

$$c = \epsilon c_1 \tag{4.4}$$

$$\phi = \epsilon \phi_1 \tag{4.5}$$

$$\alpha = \epsilon \alpha_1, \tag{4.6}$$

where r_2 , c_1 and α_1 are constants (having no ϵ -dependence). We assume that the other constants (b and γ) do not depend on ϵ . We also assume that ϕ_1 is a slowly varying function of x , varying on an $O(1/\epsilon)$ length scale, i.e. $\phi_1(x) = f(\epsilon x)$ where the definition of f does not itself depend on ϵ .

The scalings for r , ϕ and α represent small-amplitude convection, a small tilt angle, and a small up-down asymmetry, and all of these agree with the scalings made in the previous chapter (section 3.3). We choose $c = O(\epsilon)$ out of necessity; the calculation we

are about to perform would fail if c was taken to be of order 1. However, we can justify the choice of small c in terms of our linear model (Chapter 2). There, we adopted the Boussinesq approximation, with a depth-dependent κ being used to break the up-down symmetry. It turned out that the speed of travel of our solutions was proportional to the amount of up-down asymmetry (i.e. the relative size of $d\kappa/dz$). But here, we must assume small up-down asymmetry (equation 4.6), so it is consistent to take a slow speed of travel as well (equation 4.4).

Note also that by rescaling ψ and redefining ϵ , we can without loss of generality rescale α_1 and γ arbitrarily. We do so, setting $\alpha_1 = 1/2$, $\gamma = 1/3$ (this will simplify the equations later on).

Equation (4.1) becomes

$$\frac{\partial\psi}{\partial t} = \epsilon^2(r_2 + a\phi_1^2)\psi - (1 + \nabla^2)^2\psi + \frac{1}{2}\epsilon\psi^2 - \frac{1}{3}\psi^3 + \epsilon^2 c_1 \phi_1 \frac{\partial\psi}{\partial x} + b\epsilon^2 \phi_1^2 \frac{\partial^2\psi}{\partial x^2}. \quad (4.7)$$

We can make the separation of length and time scales explicit by introducing ‘fast’ variables $x' = x$, $y' = y$, $t' = t$ and ‘slow’ variables $X = \epsilon x/\sqrt{3}$, $Y = \epsilon y/\sqrt{3}$, $T = \epsilon^2 t$ (the factors of $\sqrt{3}$ are for later convenience). We now imagine ψ as being a function of both the fast and slow variables, writing $\psi = \psi(x', y', t', X, Y, T)$ instead of the previous $\psi = \psi(x, y, t)$. Using the chain rule, we find the following relationships between the old and new variables:

$$\frac{\partial\psi}{\partial t} = \frac{\partial\psi}{\partial t'} + \epsilon^2 \frac{\partial\psi}{\partial T} \quad (4.8)$$

$$\frac{\partial\psi}{\partial x} = \frac{\partial\psi}{\partial x'} + O(\epsilon) \quad (4.9)$$

$$\frac{\partial^2\psi}{\partial x^2} = \frac{\partial^2\psi}{\partial x'^2} + O(\epsilon) \quad (4.10)$$

$$-(1 + \nabla^2)^2\psi = L_0\psi + \epsilon L_1\psi + \epsilon^2 L_2\psi + O(\epsilon^3) \quad (4.11)$$

where

$$L_0 = -(1 + \nabla'^2)^2 \quad (4.12)$$

$$L_1 = -\frac{4}{\sqrt{3}}(1 + \nabla'^2) \left(\frac{\partial^2}{\partial x' \partial X} + \frac{\partial^2}{\partial y' \partial Y} \right) \quad (4.13)$$

$$L_2 = -\frac{2}{3}(1 + \nabla'^2) \left(\frac{\partial^2}{\partial X^2} + \frac{\partial^2}{\partial Y^2} \right) - \frac{4}{3} \left(\frac{\partial^2}{\partial x' \partial X} + \frac{\partial^2}{\partial y' \partial Y} \right)^2 \quad (4.14)$$

and $\nabla'^2 = \partial^2/\partial x'^2 + \partial^2/\partial y'^2$.

Note that because we assumed that ϕ varies on an $O(1/\epsilon)$ length scale, ϕ_1 can be treated as a function of X alone (and not x').

The next step is to expand ψ as

$$\psi = \epsilon\psi_1 + \epsilon^2\psi_2 + \epsilon^3\psi_3 + \dots \quad (4.15)$$

and substitute into (4.7). Equating coefficients at $O(\epsilon)$ gives

$$\frac{\partial\psi_1}{\partial t'} = L_0\psi_1. \quad (4.16)$$

We look for solutions in which $\partial\psi/\partial t' = 0$, so (4.16) simply becomes $L_0\psi_1 = 0$, which has solutions

$$\psi_1 = z(X, Y, T) \exp(ik_x x' + ik_y y') + \text{c.c.} \quad (4.17)$$

for any k_x and k_y satisfying $k_x^2 + k_y^2 = 1$, and for an arbitrary function $z(X, Y, T)$. At this stage we are free to take any linear combination of these solutions. We choose to take three modes on a hexagonal lattice, giving us the following solution for ψ_1 :

$$\psi_1 = \sum_{j=1}^3 z_j(X, Y, T) \exp(i\mathbf{k}_j \cdot \mathbf{x}') + \text{c.c.} \quad (4.18)$$

with

$$\mathbf{k}_1 = (0, -1), \quad \mathbf{k}_{2,3} = (\mp\sqrt{3}/2, 1/2). \quad (4.19)$$

(Cf. Figure 3.4 on page 72; our choice here corresponds to $\theta = 30^\circ$.)

At $O(\epsilon^2)$ we have

$$0 = L_0\psi_2 + L_1\psi_1. \quad (4.20)$$

It happens that ψ_1 , as given by (4.18), satisfies $L_1\psi_1 = 0$, hence (4.20) \Rightarrow $L_0\psi_2 = 0$. The solutions for ψ_2 are proportional to $\exp i\mathbf{k} \cdot \mathbf{x}'$, with $|\mathbf{k}| = 1$, and also satisfy

$$L_1\psi_2 = 0. \quad (4.21)$$

At $O(\epsilon^3)$ we obtain (after some rearrangement)

$$-L_0\psi_3 = -\frac{\partial\psi_1}{\partial T} + (r_2 + a\phi_1^2)\psi_1 + L_2\psi_1 + c_1\phi_1 \frac{\partial\psi_1}{\partial x'} + b\phi_1^2 \frac{\partial^2\psi_1}{\partial x'^2} + \frac{1}{2}\psi_1^2 - \frac{1}{3}\psi_1^3. \quad (4.22)$$

Here we have used (4.21).

The operator L_0 is self-adjoint, so $\langle L_0 y_1, y_2 \rangle = \langle y_1, L_0 y_2 \rangle$ for any two functions y_1 and y_2 .¹ In particular, $\langle L_0 \psi_3, \psi_1 \rangle = \langle \psi_3, L_0 \psi_1 \rangle$; and since $L_0 \psi_1 = 0$, this implies that

¹Here $\langle f, g \rangle$ is an inner product between functions f and g , defined by $\langle f, g \rangle = \int \bar{f}(x)g(x)dx$. The integral is taken over a suitable interval in x (e.g. if the functions had periodic boundary conditions, then the integral would be over one period).

$\langle L_0\psi_3, \psi_1 \rangle = 0$. The net result of this is that $L_0\psi_3$ cannot contain any terms proportional to $\exp(\pm i\mathbf{k}_j \cdot \mathbf{x}')$.

We will now, therefore, pick out terms on the right-hand side of (4.22) that are proportional to $\exp(\pm i\mathbf{k}_1 \cdot \mathbf{x}')$. (The corresponding terms with \mathbf{k}_2 or \mathbf{k}_3 in place of \mathbf{k}_1 can be obtained by cyclic permutation of indices.) We first of all note that

$$\psi_1^2 = 2\bar{z}_2\bar{z}_3 \exp(i\mathbf{k}_1 \cdot \mathbf{x}') + \text{c.c.} + \text{other terms} \quad (4.23)$$

$$\psi_1^3 = z_1(3|z_1|^2 + 6|z_2|^2 + 6|z_3|^2) \exp(i\mathbf{k}_1 \cdot \mathbf{x}') + \text{c.c.} + \text{other terms} \quad (4.24)$$

where ‘other terms’ denotes terms that are not proportional to $\exp(\pm i\mathbf{k}_1 \cdot \mathbf{x}')$. We then obtain

$$\begin{aligned} -L_0\psi_3 = & \left[-\frac{\partial z_1}{\partial T} + (r_2 + a\phi_1^2)z_1 + \frac{4}{3} \left(k_{x1} \frac{\partial}{\partial X} + k_{y1} \frac{\partial}{\partial Y} \right)^2 z_1 + c_1\phi_1 i k_{x1} z_1 - b\phi_1^2 k_{x1}^2 z_1 \right. \\ & \left. + \bar{z}_2\bar{z}_3 - z_1(|z_1|^2 + 3|z_2|^2 + 3|z_3|^2) \right] \exp(i\mathbf{k}_1 \cdot \mathbf{x}') + \text{other terms} \end{aligned} \quad (4.25)$$

where again the ‘other terms’ are not proportional to $\exp(\pm i\mathbf{k}_1 \cdot \mathbf{x}')$. Since $L_0\psi_3$ cannot contain any terms proportional to $\exp(\pm i\mathbf{k}_1 \cdot \mathbf{x}')$, the entire right-hand side of the equation (excluding the ‘other terms’) can be set to zero as a solvability condition. Doing this for the other two equations (obtained by cyclic permutation) as well, and also substituting the values of k_{xj} and k_{yj} , yields the following equations:

$$\begin{aligned} \frac{\partial z_1}{\partial T} = & (r_2 + a\phi_1^2)z_1 + \frac{4}{3} \frac{\partial^2 z_1}{\partial Y^2} \\ & + \bar{z}_2\bar{z}_3 - z_1(|z_1|^2 + 2|z_2|^2 + 2|z_3|^2) \end{aligned} \quad (4.26)$$

$$\begin{aligned} \frac{\partial z_2}{\partial T} = & (r_2 + (a - \tilde{b})\phi_1^2)z_2 - \tilde{c}\phi_1 i z_2 + \left(-\frac{\partial}{\partial X} + \frac{1}{\sqrt{3}} \frac{\partial}{\partial Y} \right)^2 z_2 \\ & + \bar{z}_3\bar{z}_1 - z_2(|z_2|^2 + 2|z_3|^2 + 2|z_1|^2) \end{aligned} \quad (4.27)$$

$$\begin{aligned} \frac{\partial z_3}{\partial T} = & (r_2 + (a - \tilde{b})\phi_1^2)z_3 + \tilde{c}\phi_1 i z_3 + \left(\frac{\partial}{\partial X} + \frac{1}{\sqrt{3}} \frac{\partial}{\partial Y} \right)^2 z_3 \\ & + \bar{z}_1\bar{z}_2 - z_3(|z_3|^2 + 2|z_1|^2 + 2|z_2|^2) \end{aligned} \quad (4.28)$$

where $\tilde{b} = 3b/4$ and $\tilde{c} = \sqrt{3}c_1/2$ (these rescalings eliminate a couple of numeric constants that would otherwise appear in the equations). Equations (4.26)–(4.28) are the three amplitude equations (Landau-Ginzburg equations) for our model.

As a simplification, we will neglect all Y -dependence in the following sections, so that $\partial/\partial Y$ can be set to zero. (This is reasonable because we do not expect to see any significant variation along the Y direction, since the coefficients of the equations are constant along the Y direction, and vary only in the X direction.)

4.3.1 Setting up the problem

In order to specify the problem fully, we have to choose a function $\phi_1(X)$, as well as giving values for r_2 , a , \tilde{b} and \tilde{c} . Initially, we will set the constants r_2 and \tilde{c} to zero, and look at the effects of non-zero values later on.

This leaves a and \tilde{b} , which affect how the growth rates for the three modes change with ϕ . For these we can refer back to the results of our steady hexagonal model, described in section 3.3. Recall that there was a pitchfork bifurcation at $\phi = \phi_{\text{pf}}$ at which rolls became stable, and also a saddle-node bifurcation at $\phi = \phi_{\text{sn}}$ at which the hexagons became unstable. In this chapter, we will scale our parameters such that $\phi_{\text{pf}} = 1$. (This can always be done by multiplying both a and \tilde{b} by ϕ_{pf}^2 if the latter is not equal to 1.) This effectively leaves one free parameter, which we may take to be $a/(a - \tilde{b})$; this is equivalent to the parameter A_1 from section 3.3.1. (This parameter measures the amount of anisotropy in the system; $A_1 = 1$ gives an isotropic system while $A_1 \gg 1$ implies a highly anisotropic problem.)

Recall also that the pitchfork bifurcation at ϕ_{pf} could be either supercritical or subcritical, depending on A_1 . We will investigate two values of A_1 , one for each of these possibilities. Case I will have

$$A_1 = 1.11, \quad a = 0.826, \quad \tilde{b} = 0.082, \quad (4.29)$$

which produces a subcritical bifurcation (with $\phi_{\text{pf}} = 1$ and $\phi_{\text{sn}} = 1.4$). Case II will be supercritical, with

$$A_1 = 2.5, \quad a = 0.391, \quad \tilde{b} = 0.234. \quad (4.30)$$

The choice of $\phi_1(X)$ defines how much the tilt varies by, and over what length scale it varies. For computational convenience we will take ϕ_1 to be a periodic function, with period X_0 , defined as follows:

$$\phi_1 = 0.75(1 - \cos(2\pi X/X_0)). \quad (4.31)$$

This function varies sinusoidally from 0 at the edges of the domain to 1.5 in the centre. We can now impose periodic boundary conditions when solving (4.26)–(4.28), with the solution domain being $X \in [0, X_0]$, or equivalently $x \in [0, L]$, where $L = X_0\sqrt{3}/\epsilon$.

With periodic boundary conditions we can easily compute solutions to (4.26)–(4.28) using a Fourier spectral method for the horizontal differences. We couple this with an ETD (exponential time differencing) method for the time discretization (Cox and

Matthews, 2002). Given values for r_2 , a , \tilde{b} and \tilde{c} , and ϕ_0 , ϕ_1 and X_0 , we can then solve the equations numerically to find z_1 – z_3 as functions of X and T .

Then, once we have the three amplitudes z_1 – z_3 , and a value for L , we can reconstruct ψ (to lowest order) from equation (4.18). In the following, we fix L to be a constant, choosing a value that gives a reasonably large number of convection cells across the width of the domain. We allow X_0 to vary; note that this is equivalent to varying ϵ , since $\epsilon = X_0\sqrt{3}/L$.

There is one other requirement before numerical calculations can be performed, which comes about because there is no diffusion term in (4.26) (after setting $\partial/\partial Y = 0$). This causes problems numerically, and we resolve this by adding a small ‘regularizing’ term, $-\eta\partial^4 z_1/\partial X^4$, to the right-hand side of (4.26), where η is chosen to be a very small value (i.e. small enough that varying η has no qualitative effect on the results). This prevents numerical difficulties and is physically reasonable, since one of the higher order terms would be a fourth-order diffusion term anyway.

4.3.2 Theoretical ideas

In the case $\tilde{c} = 0$ (in which the ‘travelling’ term is switched off), we can make some progress theoretically.

If we momentarily neglect the diffusion terms in equations (4.26)–(4.28), then there are no X -derivatives in the equations, and we are effectively left with a set of ODEs for each point along the X axis. These ODEs are nothing other than the ‘steady hexagonal’ model from the previous chapter (section 3.3). Since we know $\phi(X)$, we can use the results of that chapter (e.g. the bifurcation diagram Figure 3.8) to plot the stable solution(s) as a function of X . This has been done in Figure 4.1.

These graphs give us an idea of what the solution to the PDEs (4.26)–(4.28) will be. In the supercritical case we would expect the solution to closely follow the graphs shown in the middle row of Figure 4.1, although perhaps modified slightly by the diffusion terms in (4.26)–(4.28), which we have so far neglected. However, in the subcritical case, pictured in the top row of the figure, there are two different solution branches, and the solution to the PDEs cannot follow both of these simultaneously. There would have to be a discontinuous change (or front) between the two patterns at at least one point.

Near such a front, the diffusion terms will clearly play an important role. In fact, they have two effects: firstly, they smooth out the front, so that instead of a sharp

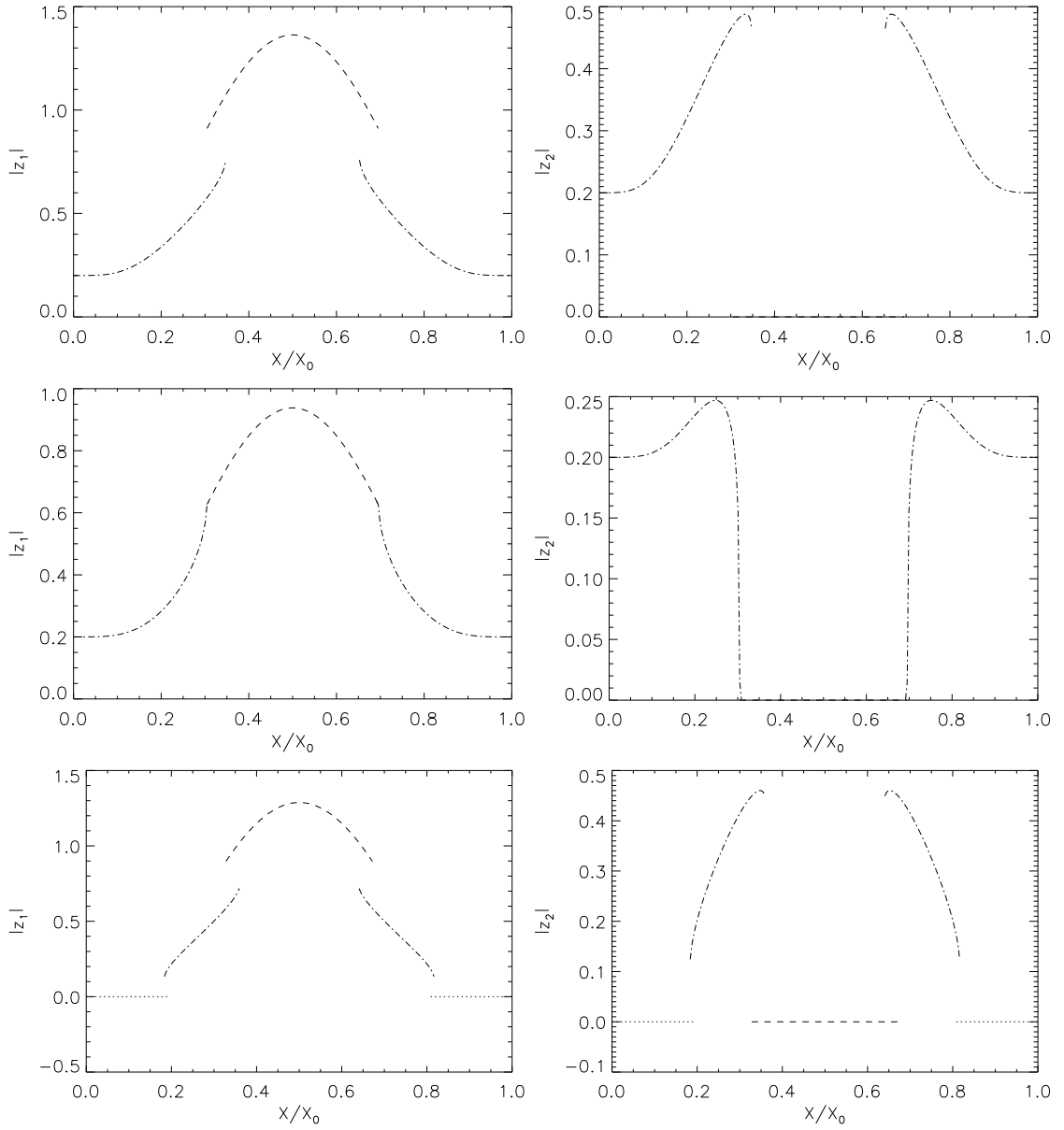


Figure 4.1: Graphs showing the stable roll (dashed line) and hexagon (dash-dotted line) branches, as well as the trivial solution (dotted line), as indicated by the analysis of section 4.3.2. The left-hand column shows $|z_1|$ against X , and the right-hand column shows $|z_2| = |z_3|$ against X . These amplitudes are only plotted at points where the respective solutions are stable. The top row is the subcritical case (see equation 4.29), the middle row is the supercritical case (equation 4.30), and the bottom row shows the subcritical case with r_2 changed to -0.2 .

discontinuity there is a continuous change over some diffusive length scale; secondly, as we will see shortly, they can actually cause the front to travel, either to the left or to the right.

We can investigate this phenomenon by considering what happens when ϕ is uniform. Although this is not the case in our model, it should nevertheless give an idea of what happens if ϕ is varying only slowly with X .

We first of all write the equations in the following form:

$$\dot{z}_1 = \frac{\partial U}{\partial z_1} \quad (4.32)$$

$$\dot{z}_2 = \frac{\partial U}{\partial z_2} + \frac{\partial^2 z_2}{\partial X^2} \quad (4.33)$$

$$\dot{z}_3 = \frac{\partial U}{\partial z_3} + \frac{\partial^2 z_3}{\partial X^2} \quad (4.34)$$

where

$$U = \frac{\mu_1}{2} z_1^2 + \frac{\mu_{23}}{2} (z_2^2 + z_3^2) - \frac{1}{4} (z_1^4 + z_2^4 + z_3^4) - (z_1^2 z_2^2 + z_2^2 z_3^2 + z_3^2 z_1^2) + z_1 z_2 z_3 \quad (4.35)$$

(here we have neglected the fourth order diffusion term in the \dot{z}_1 equation, since it is very small). U can be thought of as a ‘potential’.

We look for solutions of the form $z_j(x, t) = z_j(\xi)$, where $\xi = x - vt$, and v is a constant. These are uniformly translating solutions (i.e., they are time-independent when viewed in a frame moving with constant velocity v). The equations become:

$$-v \frac{dz_1}{d\xi} = \frac{\partial U}{\partial z_1} \quad (4.36)$$

$$-v \frac{dz_2}{d\xi} = \frac{\partial U}{\partial z_2} + \frac{d^2 z_2}{d\xi^2} \quad (4.37)$$

$$-v \frac{dz_3}{d\xi} = \frac{\partial U}{\partial z_3} + \frac{d^2 z_3}{d\xi^2}. \quad (4.38)$$

Multiplying each equation by $dz_j/d\xi$, and summing, we obtain:

$$\frac{d}{d\xi} \left[U + \frac{1}{2} \left(\frac{dz_2}{d\xi} \right)^2 + \frac{1}{2} \left(\frac{dz_3}{d\xi} \right)^2 \right] = -v \left[\left(\frac{dz_1}{d\xi} \right)^2 + \left(\frac{dz_2}{d\xi} \right)^2 + \left(\frac{dz_3}{d\xi} \right)^2 \right]. \quad (4.39)$$

If we define

$$E = U + \frac{1}{2} \left(\frac{dz_2}{d\xi} \right)^2 + \frac{1}{2} \left(\frac{dz_3}{d\xi} \right)^2, \quad (4.40)$$

then we can see that E is either an increasing function of ξ (if $v < 0$), a decreasing function (if $v > 0$), or constant (if $v = 0$).

Now consider a solution containing a front between hexagons and rolls. In particular, suppose that there are hexagons for large negative ξ , and rolls for large positive ξ , with a transition region near $\xi = 0$. In regions far from the origin, z_1 , z_2 and z_3 are constant, and so $E = U$ there. So we have $E \rightarrow U_{\text{hex}}$ for $\xi \ll 0$ and $E \rightarrow U_{\text{rolls}}$ for $\xi \gg 0$ (where U_{hex} and U_{rolls} are the potentials for the hexagon and roll solutions respectively).

Therefore, we see that if $U_{\text{hex}} > U_{\text{rolls}}$, then v will be positive, and the front will move to the right (so that the hexagons invade the rolls). If $U_{\text{hex}} < U_{\text{rolls}}$ then the opposite happens and the rolls invade the hexagons. The solution with the higher value of U ‘wins’. If $U_{\text{hex}} = U_{\text{rolls}}$, then a stationary front between the two solutions is possible.

We now consider what happens if ϕ is changing with position. This technically makes the above analysis invalid: firstly, the amplitudes in the ‘hexagon’ and ‘roll’ regions are no longer constant, but are varying with ϕ (and hence X), and secondly, the potential U now explicitly depends on X , which complicates the calculation somewhat. Nevertheless, if ϕ is varying slowly enough, then the above analysis should be at least approximately valid, and we can use it to get some ideas about what is happening. We find that U_{hex} and U_{rolls} now both depend on X (since they are functions of ϕ), and therefore v will also depend on X in general. This means that there will be some regions where the front travels to the left, some where it travels to the right, and (possibly) an ‘equilibrium’ position where the front can be stationary.

Therefore, even though there is an entire band of ϕ values in which hexagons and rolls are both (locally) stable, the front between them will be located at a well-defined position within this band; this will be the point at which the potentials U_{hex} and U_{rolls} (as defined above) are equal.

The above applies for $r \geq 0$. If $r < 0$ then there is an additional consideration: the trivial solution is now stable over part of the domain, where ϕ is sufficiently small. (This situation is illustrated in the bottom row of Figure 4.1). Note that the transition between the trivial solution and hexagons is associated with hysteresis, just as the transition between hexagons and rolls is. The arguments above can be applied equally well to a front between hexagons and the trivial solution. The trivial solution has $U = 0$, and so we would expect to see a sharp transition between the trivial solution and hexagons near the point where $U_{\text{hex}} = 0$.

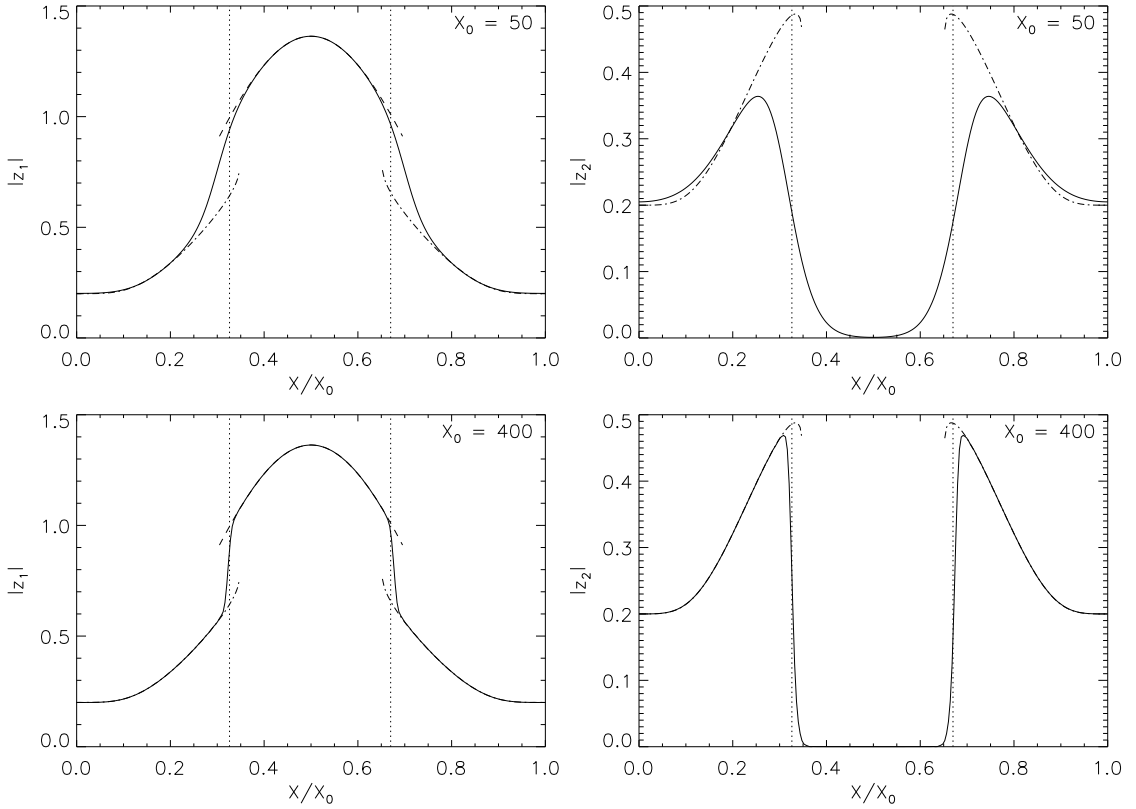


Figure 4.2: The amplitudes $|z_1|$ (left-hand column) and $|z_2| = |z_3|$ (right-hand column) corresponding to two choices for the parameter X_0 : the top row shows the case $X_0 = 50$ (corresponding to a relatively high amount of diffusion), and the bottom row shows the case $X_0 = 400$ (with much lower diffusion). The solid lines show the actual computed amplitudes. The dashed and dashed-dotted lines show the predicted stable roll and hexagon branches, respectively. The vertical dotted lines give the positions where $U_{\text{rolls}} = U_{\text{hex}}$ (see section 4.3.2).

4.3.3 Numerical results

We now discuss the results of our numerical solutions of equations (4.26)–(4.28). We will first of all look at case I (the ‘subcritical’ case, equation 4.29), and we will set $r_2 = \tilde{c} = 0$ to begin with. For our initial conditions, we set ψ to a small random value at each grid point. Initially we will take these random values to be *real*, as this simplifies the results a little; later we will move on to discuss what happens with complex initial conditions.

We begin by plotting the amplitudes $|z_1|$, $|z_2|$ and $|z_3|$ that result from such a simulation, as a function of X . This is done in Figure 4.2. We find that $|z_2|$ and $|z_3|$ end up being equal to each other, so we have plotted only two sets of graphs, one showing $|z_1|$

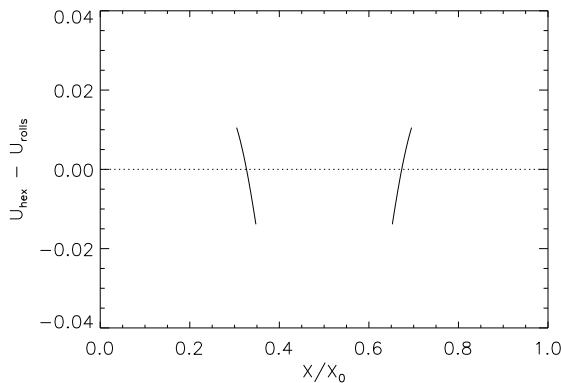


Figure 4.3: The value of $U_{\text{hex}} - U_{\text{rolls}}$ as a function of X , for the subcritical case (equation 4.29) with $r_2 = 0$. This value has been plotted only in regions where rolls and hexagons are both stable.

(left-hand column of the figure) and one showing $|z_2| = |z_3|$ (right-hand column).

The ‘ideal’ solution curves for rolls and hexagons, from Figure 4.1, are also shown, as dashed and dashed-dotted lines respectively. We find that away from the transition between rolls and hexagons, the numerical solution (solid line) follows these ideal curves quite closely. The transition itself is smoothed out over a ‘diffusion width’; this is more pronounced in the top two pictures, where there is more diffusion, than in the bottom two pictures.

We have also calculated the potentials U_{hex} and U_{rolls} (as defined in the previous section) for the parameters used in these runs. In Figure 4.3, we plot $U_{\text{hex}} - U_{\text{rolls}}$ (for those values of X where rolls and hexagons are simultaneously stable). We see that for ϕ less than a critical value, $U_{\text{hex}} > U_{\text{rolls}}$, so that the front moves towards higher ϕ ; for ϕ greater than this critical value, the opposite is true. The front therefore moves towards the critical value, which represents its stable equilibrium position. This position has been plotted on Figure 4.2 as a vertical dotted line; it can be seen that this agrees quite closely with the actual observed position of the front.

Figure 4.4 shows a representation of ψ itself for three different values of X_0 . These have been drawn at fixed $L = 40\pi\sqrt{3}$ (this value gives room for thirty hexagonal cells across the width of the box). X_0 is increasing from top to bottom; physically, increasing X_0 corresponds to reducing the amount of diffusion in the system. Unsurprisingly, the transition between rolls and hexagons is sharpest when diffusion is least (largest X_0). In fact, in this subcritical case, the sharpness of the transition is limited only by the diffusion terms.

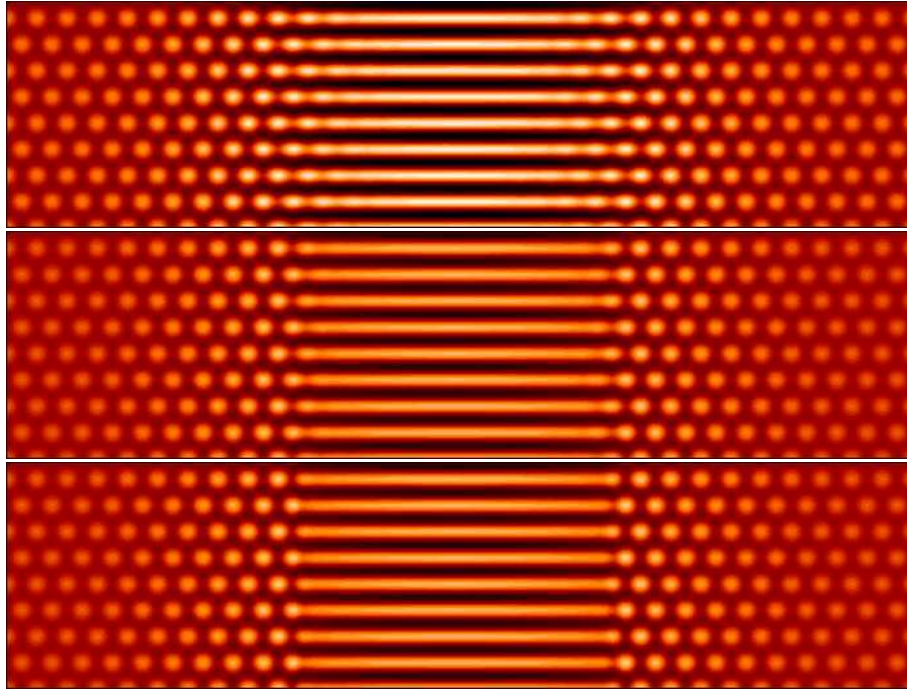


Figure 4.4: *The effect of varying X_0 (which is proportional to ϵ) in the subcritical model. The top picture shows $X_0 = 50$, the middle one $X_0 = 150$, and the bottom one $X_0 = 400$. (These are steady solutions.)*

It should also be noted that $\epsilon = X_0\sqrt{3}/L$, so increasing X_0 (at fixed L) also corresponds to increasing ϵ (our measure of the amplitude of the convection). The values of ϵ corresponding to the three panels of Figure 4.4 are 0.40, 1.19 and 3.18. These are perhaps rather large (given that ϵ is a small parameter), so the model may not strictly be valid towards the upper end of this range, but what we can conclude is that the transition becomes sharper for larger values of ϵ (which would correspond to larger Rayleigh numbers).

We also briefly mention the effect of increasing the parameter r_2 (which previously we have set to zero). Basically, this change moves the transition point between rolls and hexagons towards smaller values of ϕ (cf. Figure 3.9 on page 83). This is illustrated in Figure 4.5 where we have fixed $X_0 = 150$ and varied r_2 , taking the values 0.5, 1.2 and 1.5. As r_2 increases, the region of rolls becomes larger, until eventually rolls are seen in the entire domain.

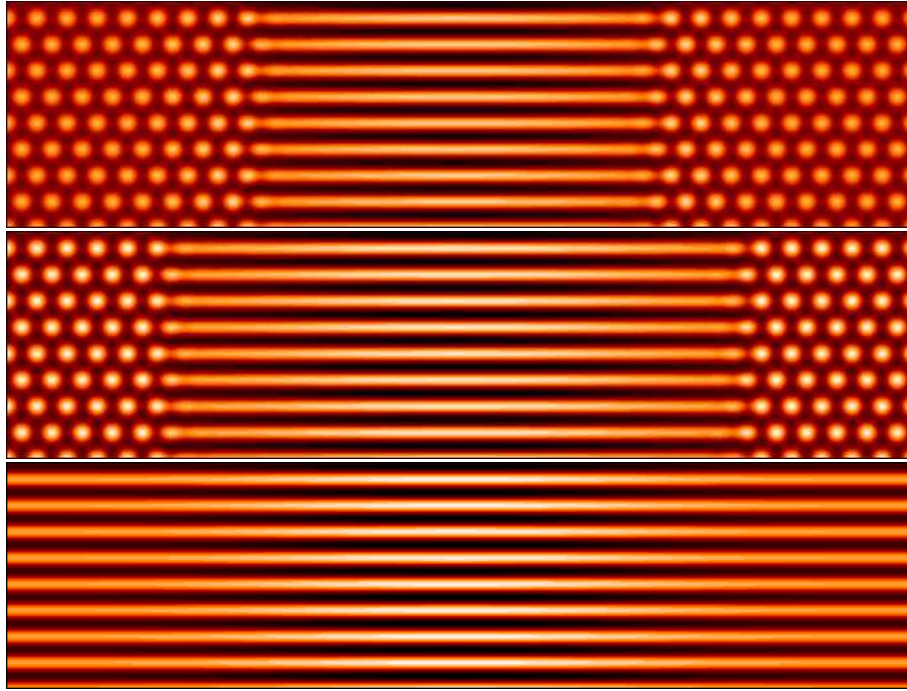


Figure 4.5: Results for (from top to bottom) $r_2 = 0.5$, $r_2 = 1.2$ and $r_2 = 1.5$. (As before, these are steady solutions.)

Results when $\tilde{c} \neq 0$

So far we have fixed $\tilde{c} = 0$; when $\tilde{c} \neq 0$ (and sufficiently large), patterns start to travel. We will choose $\tilde{c} > 0$ (without loss of generality), producing leftward-travelling patterns. This produces ‘inward’-travelling patterns on the left-hand side of the domain (corresponding to the situation in a sunspot) and ‘outward’-travelling patterns on the right-hand side.

We actually find for very small \tilde{c} that steady patterns are possible. Such a solution, for $\tilde{c} = 0.02$, is shown in Figure 4.6. For $\tilde{c} \gtrsim 0.025$, however, we find that the solutions become time-dependent, with patterns travelling to the left. Note that this travelling applies to the hexagons, but not the rolls, since \tilde{c} does not appear in the \dot{z}_1 equation.

A solution with $\tilde{c} = 0.2$ is displayed in Figure 4.7; snapshots at six different times are shown. The solution is similar in appearance to the patterns found above (with $\tilde{c} = 0$); the difference is that the hexagons now travel leftwards (although the rolls remain stationary). Moreover, the speed of this travel depends on ϕ , and hence also on X . Near the centre of the domain, the hexagons are travelling quickly, but near the left- and right-hand edges, they move more slowly. This causes the pattern to be compressed in the left-hand half of the domain, or stretched in the right-hand half, in a kind of

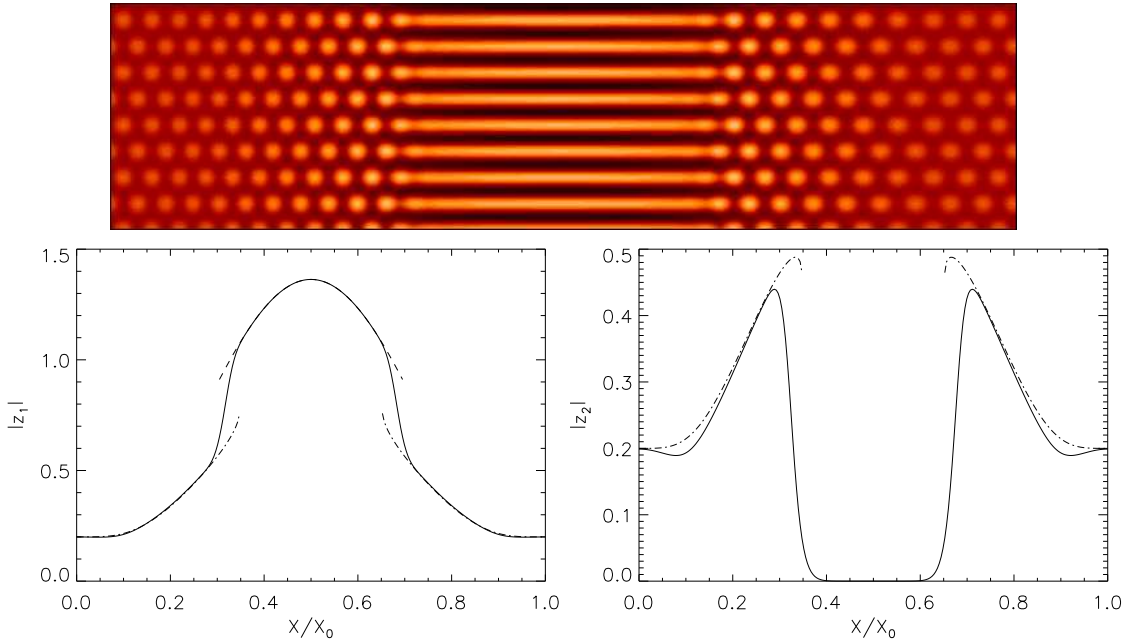


Figure 4.6: A steady solution for $\tilde{c} = 0.02$. Plots of $|z_1|$ and $|z_2| = |z_3|$ against X are also shown.

‘concertina effect’.

The small arrows on Figure 4.7 indicate points where this ‘concertina effect’ has become quite pronounced. Notice that in this situation, the wavenumber of the hexagonal pattern is now some distance away from the preferred wavenumber. The system responds to this by causing two of the ‘compressed’ hexagons join together to become one larger cell, or one ‘stretched’ hexagon to split into two smaller convection cells. After this point, the system evens itself out, with all the hexagons returning to a similar size.

This process can also be seen by looking at the amplitudes $|z_1|$ and $|z_2| = |z_3|$. These are plotted at four different times in Figures 4.8 and 4.9. To explain what’s happening here, we consider the following (linear) model equation:

$$\dot{z} = r_2 z + i\tilde{c}\phi(x)z + D \frac{\partial^2 z}{\partial x^2}. \quad (4.41)$$

This can be seen as a simplification of either (4.27) or (4.28), where only three of the right-hand-side terms have been kept. (The coefficient D is assumed to be real and positive.)

Substituting $z = R(x) \exp(i\theta(x))$ (where R and θ are real) we obtain

$$\dot{R} = (r_2 - D\theta'^2)R + DR'' \quad (4.42)$$

$$\dot{\theta} = \tilde{c}\phi(x) + 2D \frac{R'\theta'}{R} + D\theta''. \quad (4.43)$$

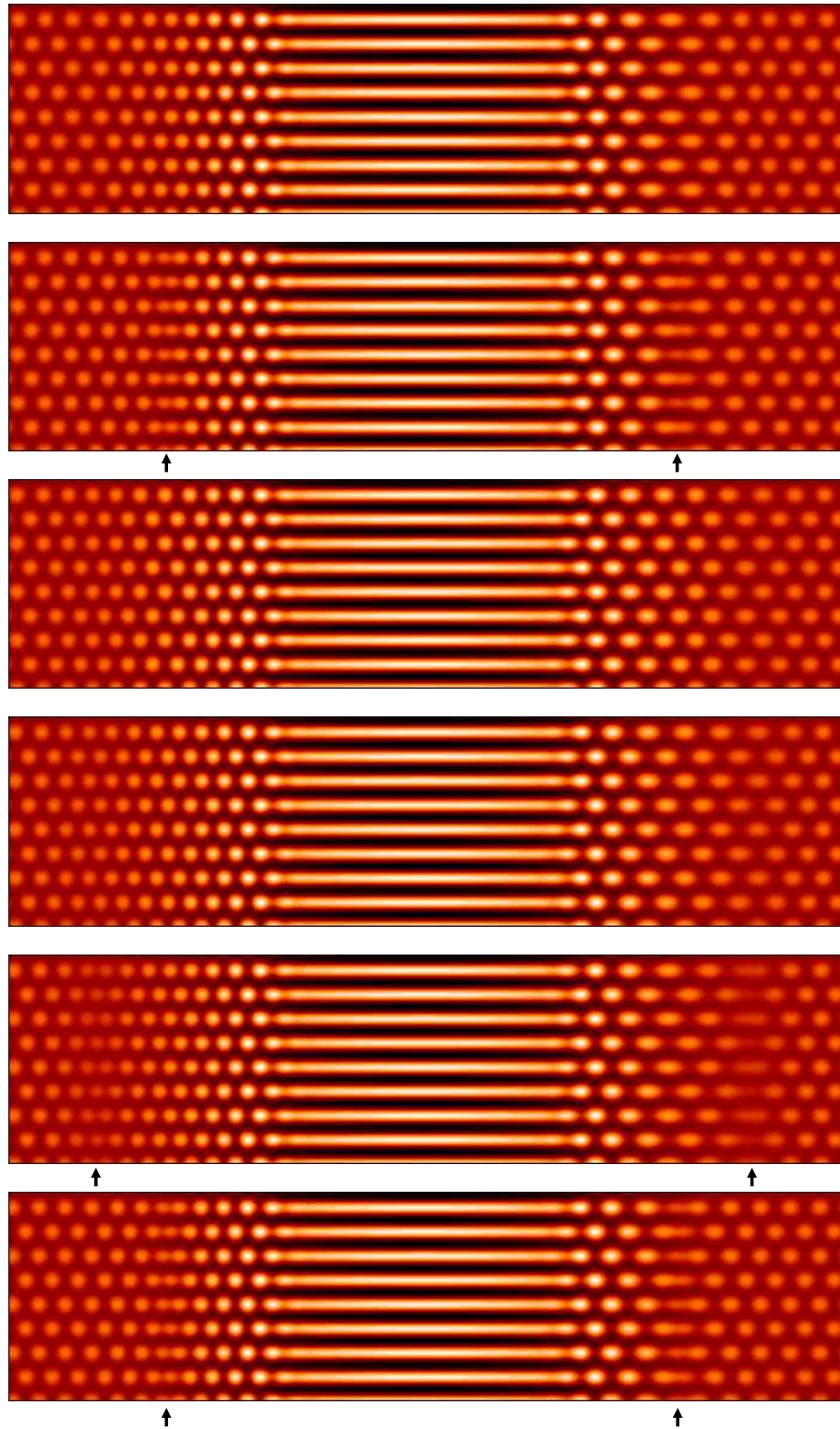


Figure 4.7: Solution for $\tilde{c} = 0.2$. Snapshots are shown every 20 time units. The arrows indicate points where the hexagons become distorted and the amplitude falls.

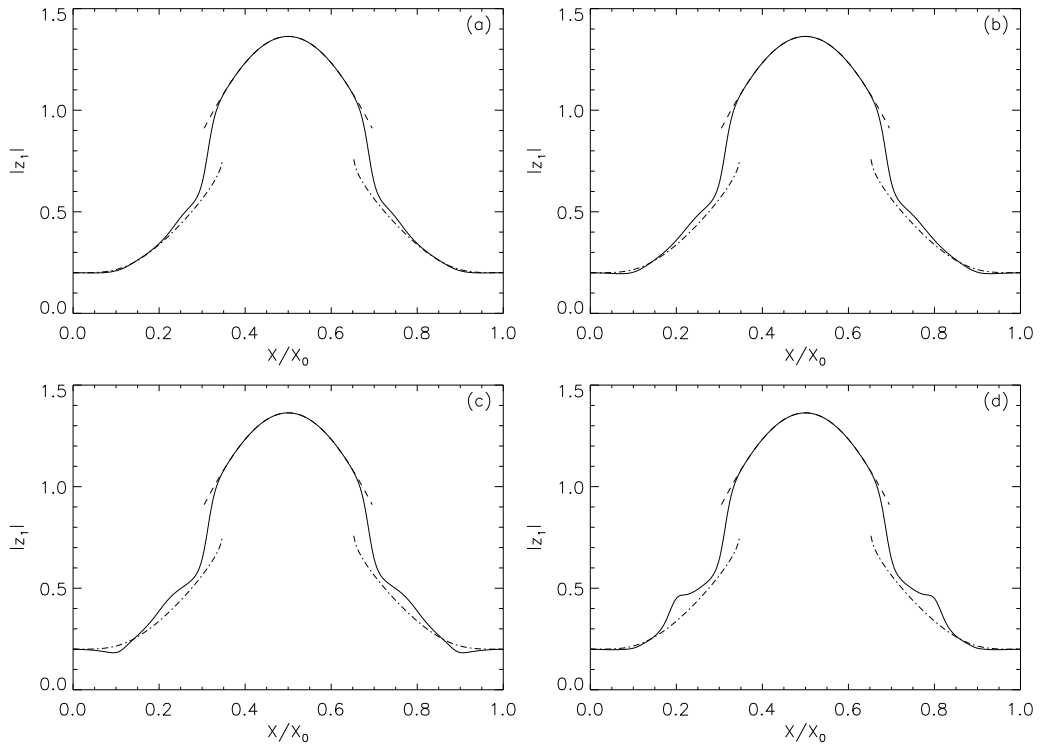


Figure 4.8: Plots of $|z_1|$ against X for the case $\tilde{c} = 0.2$. The four graphs (a)–(d) correspond to the bottom four frames from Figure 4.7.

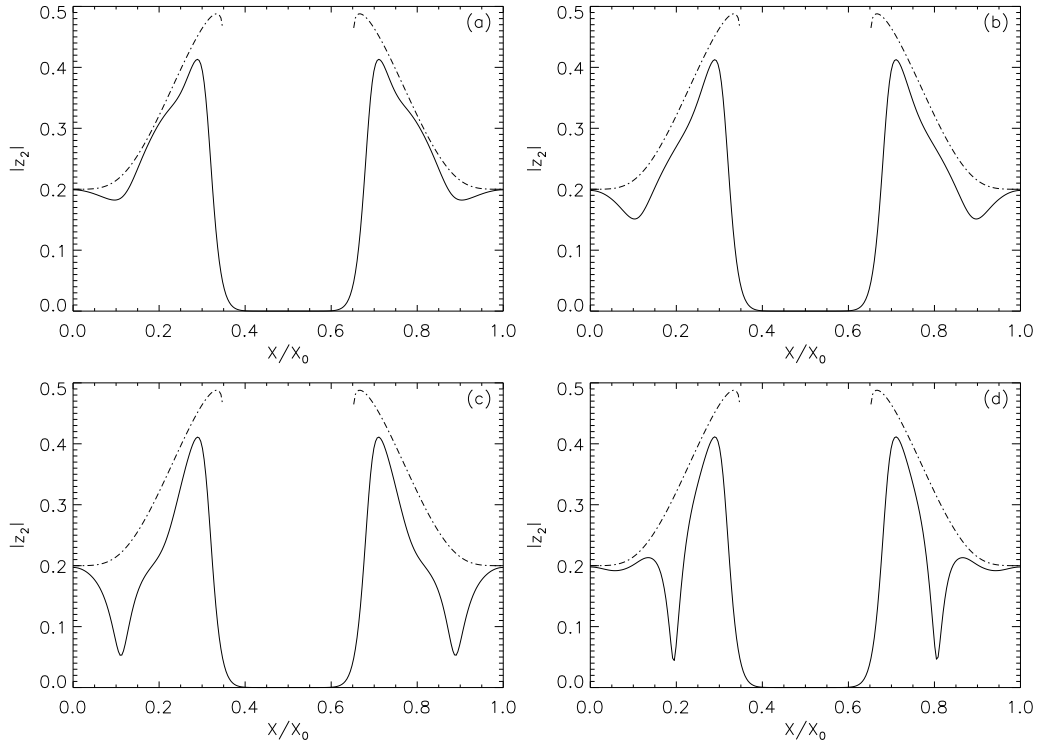


Figure 4.9: As Figure 4.8, but showing $|z_2| = |z_3|$ instead of $|z_1|$.

Equation (4.43) shows that θ increases linearly with time, at a rate proportional to $\tilde{c}\phi(x)$. This rate of increase depends on x , so the phase is ‘wound up’ over time, and gradients θ' develop.

Equation (4.42) shows that R evolves according to a diffusion equation, with a linear growth term proportional to $r_2 - D\theta^2$. Therefore, R usually grows exponentially, but if $|\theta'|$ is large enough it can start *decaying* exponentially.

Note that θ' represents a shift of the wavenumber of the basic pattern: the preferred value of the wavenumber is 1, but if θ' is nonzero then this is shifted to $1 + \theta'$. Therefore, if θ' is large, the pattern has been stretched or compressed by a large amount. (This corresponds to the ‘concertina effect’ mentioned above.) The wavenumber will be far away from its preferred value, and such modes will quickly decay.

Thus our picture is that the phases of z_2 and z_3 are ‘wound up’ with time, until eventually the wavenumber gets so far from critical that z_2 and z_3 decay sharply. This can be seen on Figures 4.9(c) and 4.9(d). By contrast, z_1 is not directly affected (since the $\tilde{c}\phi$ term does not appear in the \dot{z}_1 equation), so we see on Figure 4.8 that $|z_1|$ does not change a great deal during the evolution.

It can be seen, therefore, that this stretching and compression process has the effect of turning hexagons into rolls, with z_1 nonzero but z_2 and z_3 both very small. However, once we get close to this roll solution, we cannot stay there for long, because rolls are unstable to hexagons (at this value of X). Therefore the amplitudes $|z_2|$ and $|z_3|$ grow exponentially, and the system returns once again to hexagons (close to the critical wavenumber), restarting the cycle.

A similar pattern of motion is observed for all \tilde{c} values up to about 0.9. For smaller \tilde{c} , e.g. 0.1, the ‘concertina effect’ is observed at one value of X only, and the pattern repeats with a regular period; for larger \tilde{c} , the solution is more erratic and the ‘concertina effect’ is observed at multiple values of X .

For $\tilde{c} \gtrsim 0.9$ a different solution is observed. The system reaches a ‘quasi-steady’ state, where the amplitudes $|z_j|$ are all unchanging with time, and only the phases are time-varying. An example of such a solution (for $\tilde{c} = 1$) is shown in Figure 4.10. The hexagons in this picture travel, but only very slowly; they also expand slightly in wavelength as they move from right to left. As \tilde{c} is increased further, this state remains (values of \tilde{c} up to 20 were checked); the only change is that the region of hexagons shrinks slightly and the region of rolls expands slightly as \tilde{c} is increased.

Notice here that the rolls exist for a much larger range of X than they usually do, even

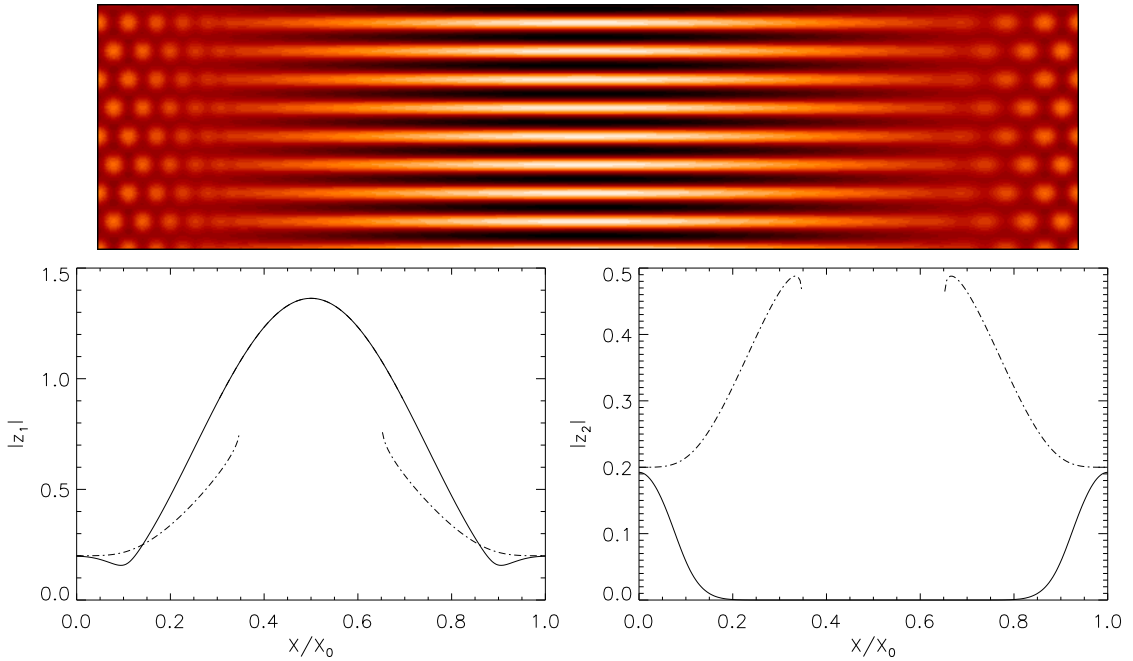


Figure 4.10: Quasi-steady solution for $\tilde{c} = 1$. The pattern is steady apart from a slow drift of the hexagons from right to left.

persisting in areas where only the hexagon branch is supposed to be stable. Although it is still true that perturbations to rolls would grow exponentially, these perturbations would also be affected by the $c_1\phi_1$ terms in equations (4.27) and (4.28). For large enough $c_1\phi_1$ it seems likely that the perturbations would be quickly ‘sheared’ away by these terms, before they had time to grow large enough to disrupt the roll solution. Therefore, it appears that the instability leading from rolls to hexagons cannot develop in regions where $c_1\phi_1$ is too large.

Additional results

Up until now we have used initial conditions consisting of purely real values for the amplitudes. We now consider the more general case of a complex initial perturbation. The results for three different values of \tilde{c} are shown in Figure 4.11. The first panel shows the result for $\tilde{c} = 0$, which is similar to the previous result (cf. Figure 4.4), except that the rolls are now slightly curved. This curvature is a relic of the initial condition and eventually fades away by diffusion, although it takes rather a long time to disappear completely, because the diffusion term in the z_1 equation is fourth order with a small diffusion coefficient.

The second panel in Figure 4.11 shows the case $\tilde{c} = 0.5$, which is again similar to

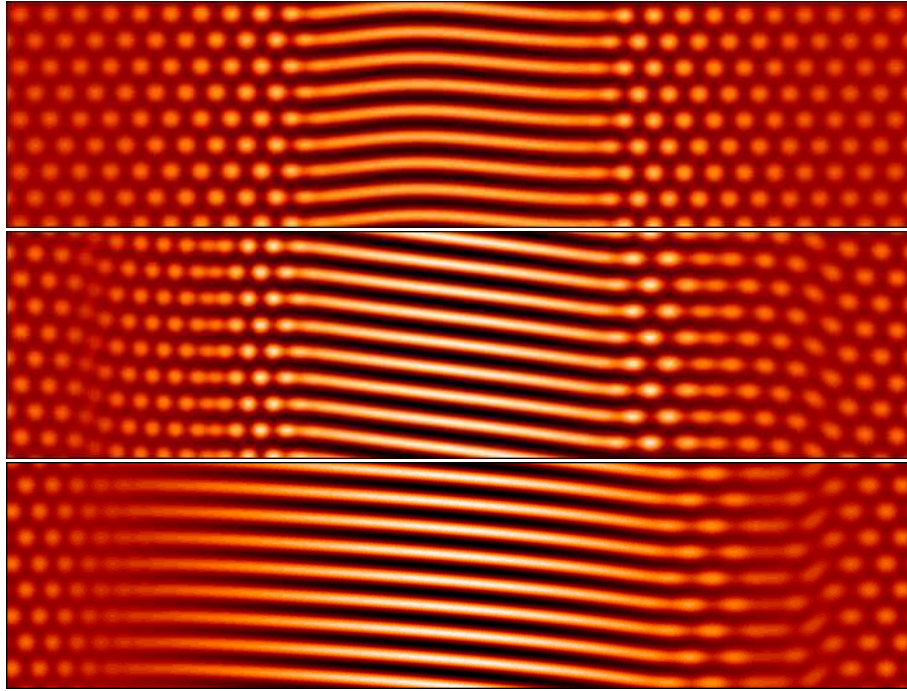


Figure 4.11: *The effect of using a complex initial condition instead of a real one. Top: $\tilde{c} = 0$, middle; $\tilde{c} = 0.5$; bottom: $\tilde{c} = 1$. As usual, the roll patterns are steady, but the hexagonal patterns travel from right to left.*

the previous results, although there is now a slightly more complicated pattern, with the possibility of curvature in both the rolls and the hexagons, as well as rolls which are not perfectly aligned with the x -axis. Finally, the bottom panel shows the case $\tilde{c} = 1$, which can be compared to Figure 4.10; the main difference here is that the rolls appear to ‘break up’ into a stretched-out cellular pattern at the right-hand side of the domain (with the left-hand side being largely unchanged).

We also briefly discuss what happens when the transition between rolls and hexagons is supercritical rather than subcritical. (This corresponds to case II, or equation 4.30, from section 4.3.1.) This is illustrated in Figure 4.12, which is the equivalent of Figure 4.4 for this case. Notice that the transition between rolls and hexagons is less sharply defined in this supercritical case (as expected); however, the difference is not all that noticeable, since the transition tends to be smoothed out by diffusion. (This does depend on our choice of ϕ though: if we chose ϕ to vary very slowly, then in the supercritical case we would see a very broad transition from rolls to hexagons, while in the subcritical case, the transition region would remain narrow. In other words, in the supercritical case the width of the transition depends directly on how quickly ϕ changes, whereas in the subcritical case the width of the transition depends only on the amount of diffusion

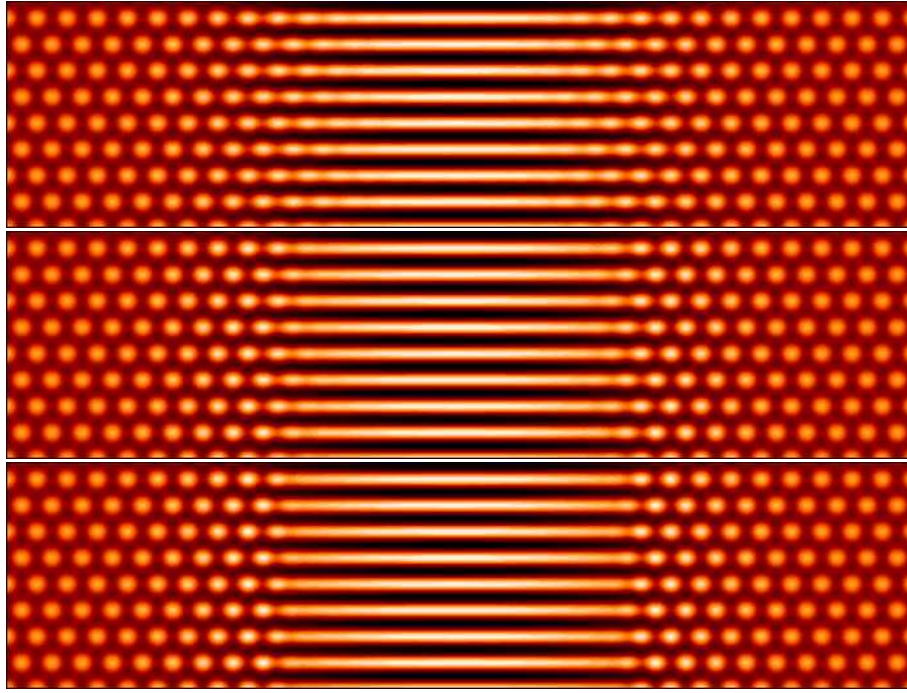


Figure 4.12: The equivalent of Figure 4.4 for the supercritical case. Notice how the transition is not quite so sharply defined as before.

in the system.)

The effects of varying ϕ

We have also looked at varying our function $\phi_1(X)$, which describes how the tilt angle varies with position. Instead of (4.31), we now use the following slightly more general definition:

$$\phi_1 = \frac{\phi_{\text{centre}}}{2} \left(1 - \cos \left(\frac{2\pi X}{X_0} \right) \right). \quad (4.44)$$

The previous definition corresponds to $\phi_{\text{centre}} = 1.5$.

So far all of our solutions have contained hexagons at the edges of the domain and rolls in the centre. This is the general situation for sufficiently large ϕ_{centre} . The other generic possibility occurs for small ϕ_{centre} and here we simply get hexagons throughout the entire domain.

There is also hysteresis between these two possibilities: both types of solution can be stable simultaneously for certain values of ϕ_{centre} . For example, this occurs for $\phi_{\text{centre}} = 1.18$, as illustrated in Figure 4.13. Here, both rolls and hexagons are stable solutions when $\phi = \phi_{\text{centre}}$, so it is possible to have either hexagons or rolls at the centre of the domain, while at the edges, the solution is always hexagons (since $\phi = 0$ at the edges of

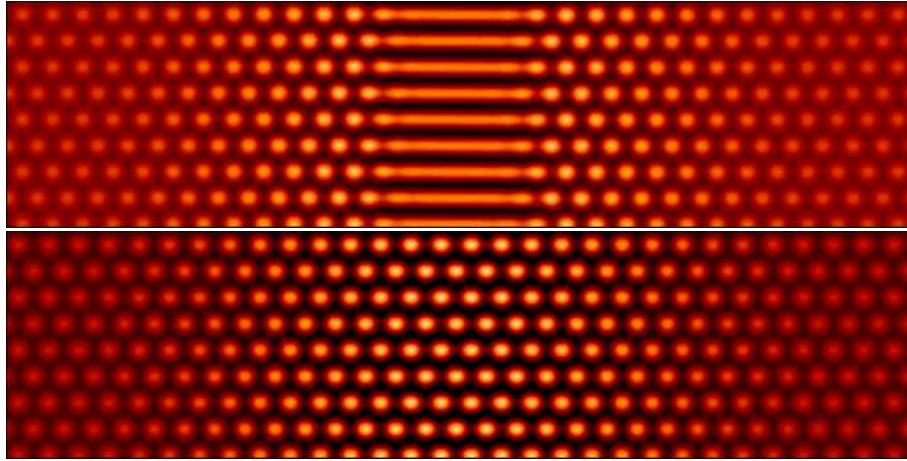


Figure 4.13: *Two possible stable solutions with $\phi_{\text{centre}} = 1.18$, $r_2 = 0$ and $\tilde{c} = 0$. (These are both steady solutions.)*

the domain). This leads to the two possible solutions shown in Figure 4.13; depending on the initial conditions, either of these two solutions can be obtained.

These results were obtained by setting $\tilde{c} = 0$. However, it appears that this hysteresis effect disappears once we take $\tilde{c} \neq 0$. In this case, only the upper solution of Figure 4.13 can be obtained (at least for long times). This is because of the distortion effect mentioned in section 4.3.3. As discussed there, the hexagons become stretched or compressed, because of the variation of the speed of travel with position, and eventually they are transformed into rolls. However, this time, rolls are actually stable in the centre of the domain, so the rolls do not turn back into hexagons again. Therefore, if we use the lower solution from Figure 4.13 as an initial condition, then it will be transformed into the upper solution from the same Figure, if \tilde{c} is non-zero. This is illustrated in Figure 4.14 for $\tilde{c} = 0.3$.

4.4 Numerical simulations of the full Swift-Hohenberg equation

We have also performed some simulations of the full Swift-Hohenberg equation (4.1). This model has more degrees of freedom than the Landau-Ginzburg equations (4.26)–(4.28), in a sense, because in the Swift-Hohenberg model the hexagonal lattice can be aligned at any angle, while in the Landau-Ginzburg model a particular orientation of the lattice has been assumed (see equation 4.19).

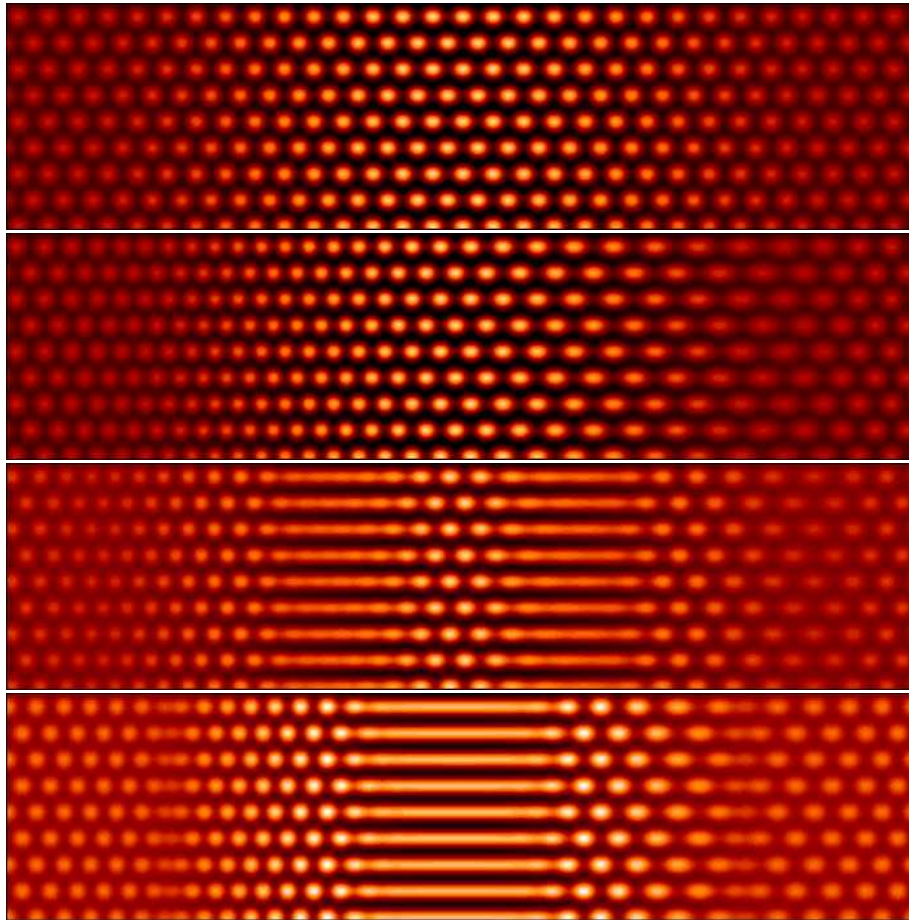


Figure 4.14: Sequence showing how the hexagons evolve into rolls when $\phi_{\text{centre}} = 1.18$, $r_2 = 0$ and $\tilde{c} = 0.3$. The top panel shows the initial condition and subsequent images show snapshots every 100 time units.

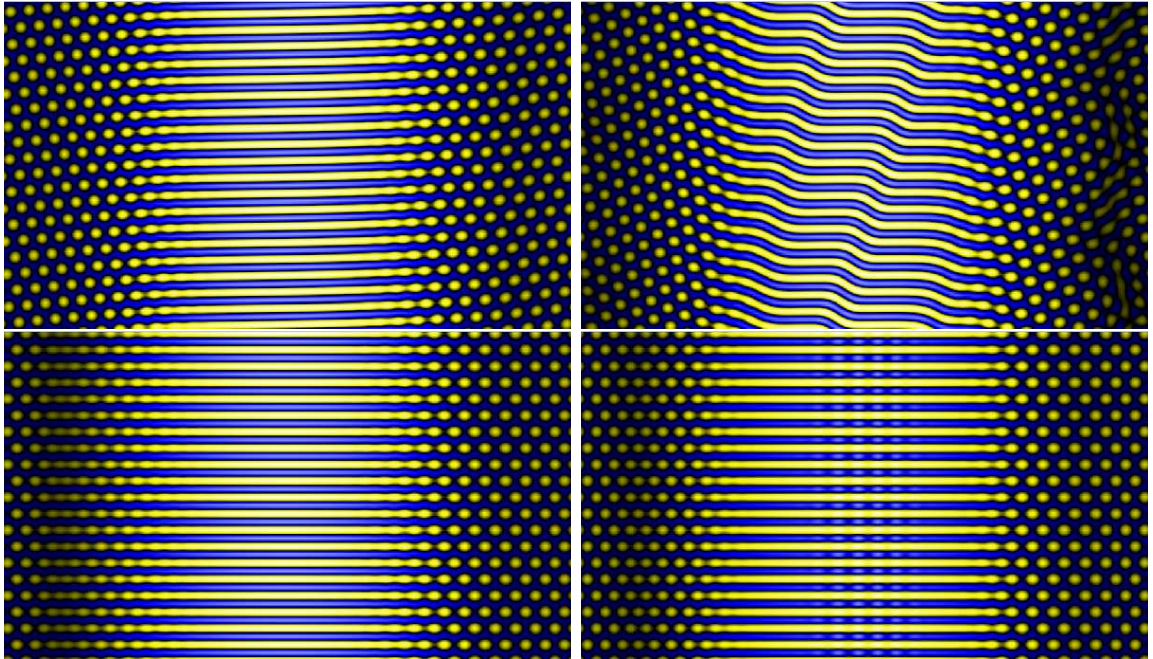


Figure 4.15: Four results from the full Swift-Hohenberg equation in rectangular geometry. The top two pictures correspond to a random initial condition, with $\tilde{c} = 0.2$ (left) and $\tilde{c} = 0.3$ (right). The bottom two pictures have a specially chosen initial condition in order to produce patterns aligned with the x axis (both with $\tilde{c} = 0.4$). The bottom right picture has a larger value of ϵ , illustrating the ‘cross rolls’ that appear at the centre in this case. Note that the hexagon patterns travel from right to left. The rolls are steady, except in the top-right hand case, where the ‘steps’ in the rolls travel leftwards.

We first look at the results in a rectangular (Cartesian) domain. In this case the results should agree with the Landau-Ginzburg model in the limit of small ϵ . In section 4.4.2 we extend the model to allow us to look at circular domains, in order to produce a better representation of real pores and sunspots (which are usually roughly circular in shape). The computations were all carried out using a modification of a code provided by S. Houghton.

4.4.1 Cartesian geometry

Figure 4.15 shows typical results in a Cartesian domain. (The parameters a and \tilde{b} were chosen as in ‘Case I’ described in section 4.3.1; we fixed $r = 0$ and looked at several values of \tilde{c} .) If ϵ is small then the results should agree with those found above (for the

Landau-Ginzburg model); the first three pictures in Figure 4.15 have $\epsilon = 0.3$ and we do indeed find similar results. However, for ϵ greater than about 0.4 to 0.5, ‘cross rolls’ start to appear at the centre of the domain (see bottom right hand picture in Figure 4.15, where $\epsilon = 0.5$). These were not seen earlier, and they might represent some sort of instability of the convection rolls. However, they could also be artifacts caused by the large value of ϵ (this model is only strictly speaking valid for small ϵ), so we must be careful in interpreting them.

Note that in the bottom two pictures, a specially chosen initial condition was used, designed to give patterns aligned with the x axis. This is the equivalent of taking a *real* initial condition in the Landau-Ginzburg model, and we indeed get good agreement with those cases. In the top two pictures of Figure 4.15, a general, random initial perturbation was used. This case does not directly correspond to the Landau-Ginzburg equations, since it tends to produce a randomly aligned lattice – and not one aligned with the x axis, as assumed in the previous model (see equation 4.19). Nevertheless, the results are similar, with a transition between hexagons at the edges and rolls in the centre of the domain, as before. One striking feature is that the rolls always manage to align themselves with the x axis (parallel to the tilt of the magnetic field), even sometimes producing a curious ‘stepped’ structure in order to achieve this (see top right picture of Figure 4.15).

4.4.2 Cylindrical geometry

We have also produced an extension of the model (4.1) in which the magnetic field’s tilt angle takes on a two-dimensional character. In other words, instead of simply imagining the field to be tilted in the x -direction, we allow the field to be tilted in any horizontal direction. This can be modelled in a simple way by allowing the ‘tilt angle’ (ϕ in the above) to become a two-dimensional vector rather than a scalar, indicating a direction as well as amount of tilt. Equation (4.1) then becomes

$$\frac{\partial \psi}{\partial t} = r\psi - (1 + \nabla^2)^2 \psi + \alpha \psi^2 - \gamma \psi^3 + a|\phi|^2 \psi + b(\phi \cdot \nabla)^2 \psi + c\phi \cdot \nabla \psi. \quad (4.45)$$

This equation can now be simulated within a circular domain, with the magnetic tilt direction pointing radially outwards. This circular configuration is more like a sunspot or pore than our previous model, which captured the behaviour of the convection in inclined fields, but not the particular geometry of a sunspot. We expect this extension of the model to give qualitatively similar results, with a travelling pattern of hexagons

and a transition to rolls for larger tilt angles, although there might now be additional effects due to the new geometry.

It is unclear what boundary conditions should be taken around the circumference of the domain. However, since this is intended to be an idealized, qualitative model only, we will simply choose illustrative boundary conditions, namely either Dirichlet ($\psi = 0$) or Neumann ($\partial\psi/\partial r = 0$) conditions at the outer edge. The use of two different boundary conditions allows us to check which results are robust and do not depend on effects at the outer boundary.

Initial results

We chose ϕ to be a radial vector: $\phi = f(r)e_r$, with $f(r)$ varying linearly from 0 at the centre to 2.3 at the outer edge of the domain. This choice allows both rolls and hexagons to appear. (The other parameters were taken from ‘Case I’ described in section 4.3.1, with $r = 0$.) The results, for four different values of \tilde{c} , are shown in Figure 4.16. These results were obtained using the Dirichlet boundary condition, but we found no qualitative differences when the Neumann boundary condition was used instead.

The four results are actually fairly similar to each other. There is a transition from hexagons at the centre (where ϕ is small) to radial rolls around the edge (where ϕ is large), as expected. For the $\tilde{c} = 0$ case, the pattern is steady and time-independent (after an initial transient); for $\tilde{c} > 0$, the hexagons travel inward, while the rolls are more or less steady and unchanging. The rolls contain a number of dislocations, which arise because of the circular geometry. If we simply had a radial pattern of rolls, with no dislocations, then the wavelength of the rolls would be increasing with radius; however, the rolls have a preferred wavelength of 2π , and so this would not be an optimal solution. Instead, dislocations are formed, and extra rolls are created, to keep the wavelength close to 2π .

Notice that the boundary between rolls and hexagons is not a perfect circle at some particular radius. Instead, the boundary is slightly blurred and ill-defined, and is irregular in shape (particularly for smaller \tilde{c}). When $\tilde{c} > 0$ the boundary is also somewhat dynamic, with patterns near the boundary constantly changing from rolls to hexagons and back again.

This irregularly-shaped boundary is a little puzzling, given that our calculation in section 4.3.2 predicted that the front would be located at a particular, well-defined value of ϕ , which in the present model would correspond to a circle at a particular

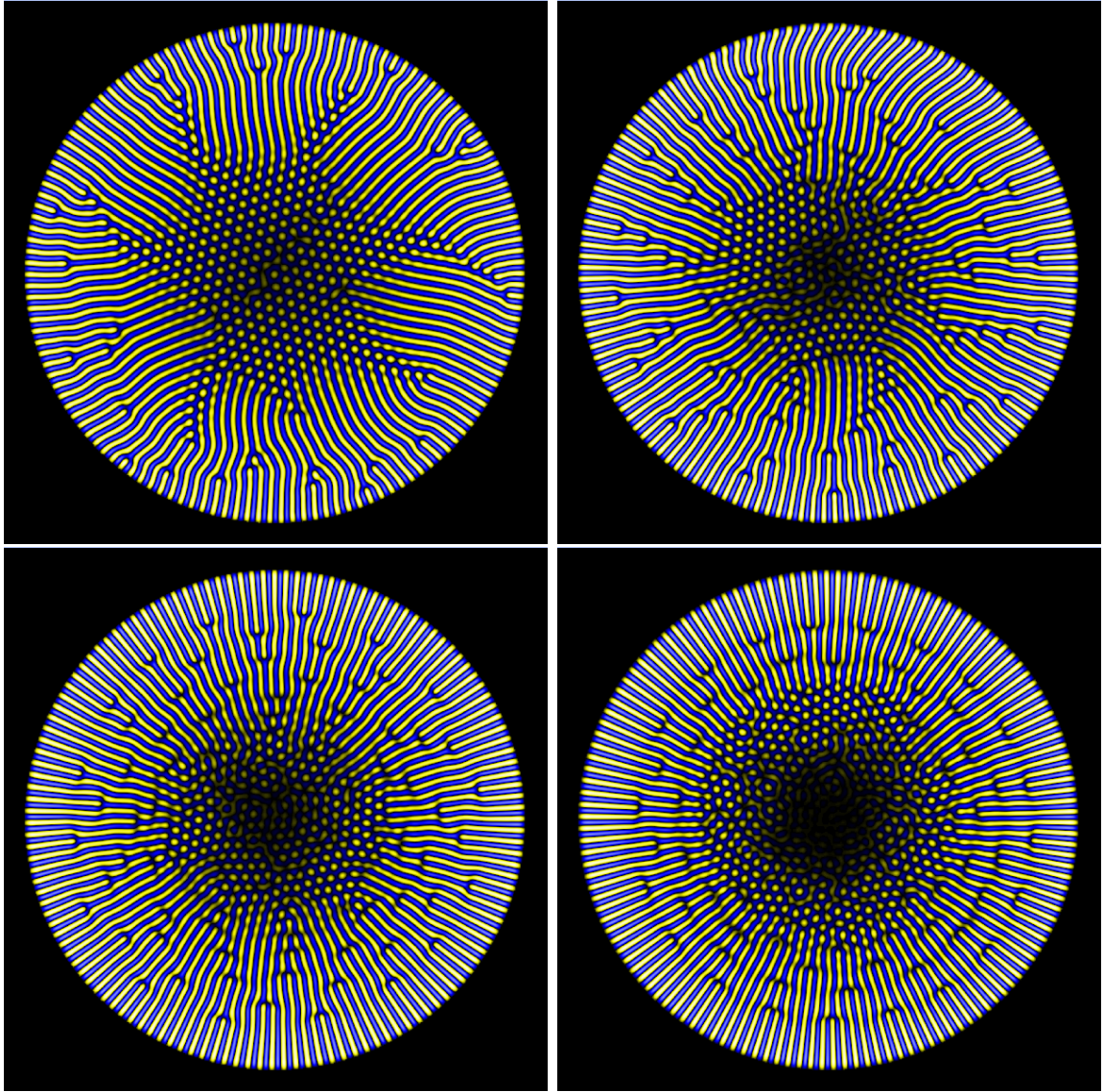


Figure 4.16: Results from the cylindrical model (equation 4.45). Top left: $\tilde{c} = 0$; top right: $\tilde{c} = 0.3$; bottom left: $\tilde{c} = 0.6$; bottom right: $\tilde{c} = 1.2$. In these pictures, the rolls are steady, while the hexagon pattern is time-dependent (with individual hexagons travelling towards the centre).

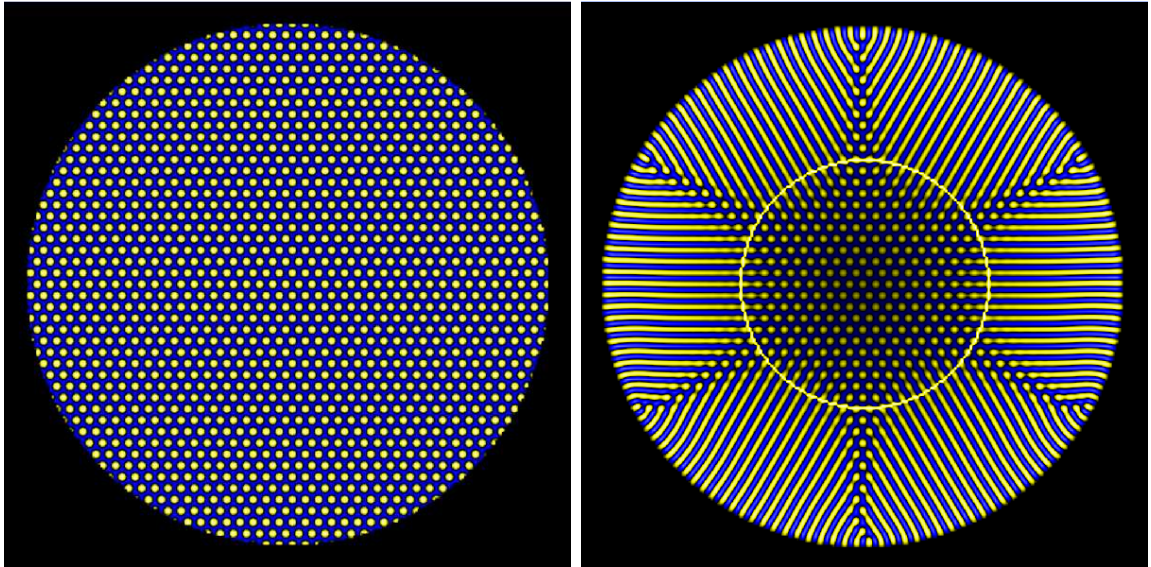


Figure 4.17: Results with $\tilde{c} = 0$ and with a specially chosen initial condition (left), designed to give a particular alignment of the hexagonal lattice. The final state is shown on the right. (These are both steady solutions.) The circle shows the expected position of the front between rolls and hexagons, based on the calculations in section 4.3.2.

radius. However, note that in that calculation, a certain particular alignment between the hexagonal lattice and the magnetic tilt vector was assumed. The rolls had to be aligned along the tilt vector and so did the hexagonal lattice (see equation 4.19). In the present results (e.g. Figure 4.16, top left picture), this condition is not always satisfied; the angle between the hexagonal lattice and the magnetic tilt direction changes with position. We can assume that the location of the front will also vary slightly, depending on this angle. Therefore, we end up with an irregularly shaped front, whose radius depends on position, as seen in the results.

As a way of illustrating this point, we have produced a result using a much more regular initial condition, shown in Figure 4.17, left-hand panel. (Note also that we set $\tilde{c} = 0$ for this result, in order to prevent any travelling wave effects from destroying the regularity of the pattern.) The initial condition is stable in the centre but unstable at the circumference of the domain, so the system rapidly evolves into the steady state shown in the right-hand panel of Figure 4.17.

Notice how the final pattern is now much more regular and symmetric than in the previous results. Correspondingly, the front between hexagons and rolls also has a much more regular structure than before. The position of the front now agrees well with the

predicted position (based on the Landau-Ginzburg calculation of section 4.3.2), which has been plotted as a circle on Figure 4.17.

Increasing the domain size with time

An interesting experiment is to allow the radius of the domain, as well as the corresponding tilt angle at the outer edge, to increase with time. This can be thought of as modelling a pore that is slowly growing with time; initially, it will contain cellular, hexagon-like convection, but once the radius goes above a certain value, the tilt angle at the outer edge will become large enough to allow rolls to appear. To model this situation we have taken our usual distribution for ϕ ($\phi = \phi_0 r e_r$, with ϕ_0 left constant) but have allowed r_{\max} to grow with time. We take a linear growth with $r_{\max} = r_0 + r_1 t$.

We ran this calculation using three different values of r_1 and with a fixed value for \tilde{c} of 0.3. A typical result is shown in Figure 4.18. Circles have also been plotted on the diagram, at radii corresponding to $\phi = \phi_{\text{pf}}$ and $\phi = \phi_{\text{sn}}$ (based on the calculations of the previous chapter), so that rolls are stable outside the outer circle, hexagons are stable inside the inner circle, and both patterns are stable in between the two circles. (Note however that the values of ϕ_{pf} and ϕ_{sn} will vary slightly, depending on the chosen orientation of the lattice – the variable θ from the previous chapter – and so the circles should be taken as a guide only.)

When the domain is small, we find a solution consisting only of hexagons (e.g. top left picture in each case), and when the domain grows larger, the solution has hexagons in the centre and rolls around the edge (e.g. bottom left and bottom right pictures). We might identify the former as a ‘pore-like’ solution and the latter as a ‘sunspot-like’ solution.

Note that one might expect the transition from hexagons to rolls to occur as ϕ increases through ϕ_{sn} , i.e. as the boundary moves through the outermost of the two circles plotted on the diagrams. In other words, we might expect the solution to follow the hexagon branch until the very end, only switching to rolls after the hexagons finally become unstable. However, this appears not to happen. Instead, the rolls seem to appear as soon as ϕ reaches ϕ_{pf} , i.e. as the boundary moves through the innermost circle, as seen in the top right picture of Figure 4.18. The reason for this is unclear, but it might be due to boundary effects which cause the roll pattern to be favoured near the boundary.

We have also performed runs in which the domain shrinks with time instead of ex-

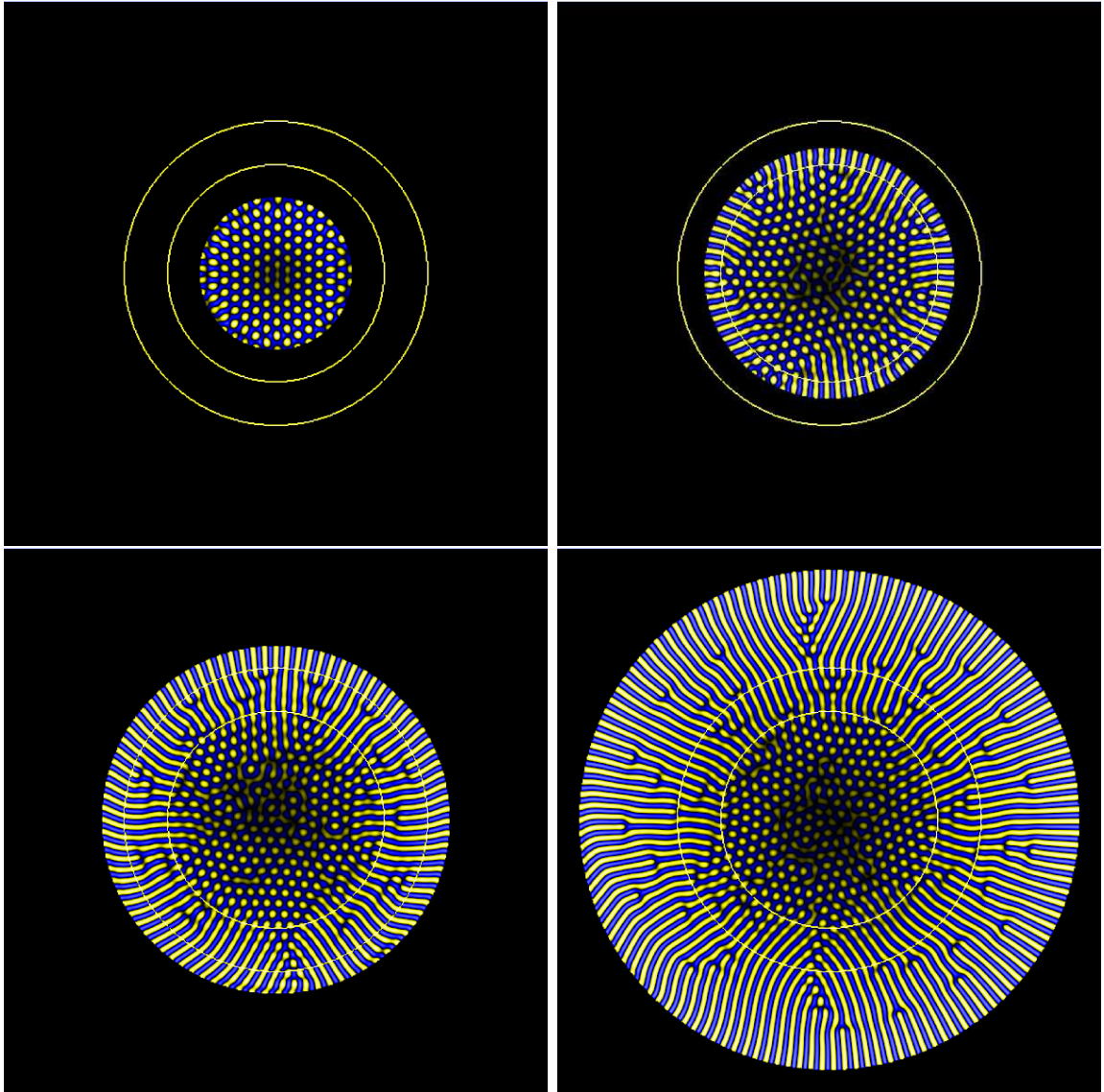


Figure 4.18: A run in which the radius of the domain has been allowed to increase slowly with time. (Snapshots are shown at four different times, with time increasing from left to right and top to bottom.) The Neumann boundary condition has been used. The two circles indicate the radii at which $\phi = \phi_{\text{pf}} = 1$ and $\phi = \phi_{\text{sn}} = 1.4$. Note that the rolls first appear (roughly) as the boundary expands through the innermost circle (see top right hand picture).

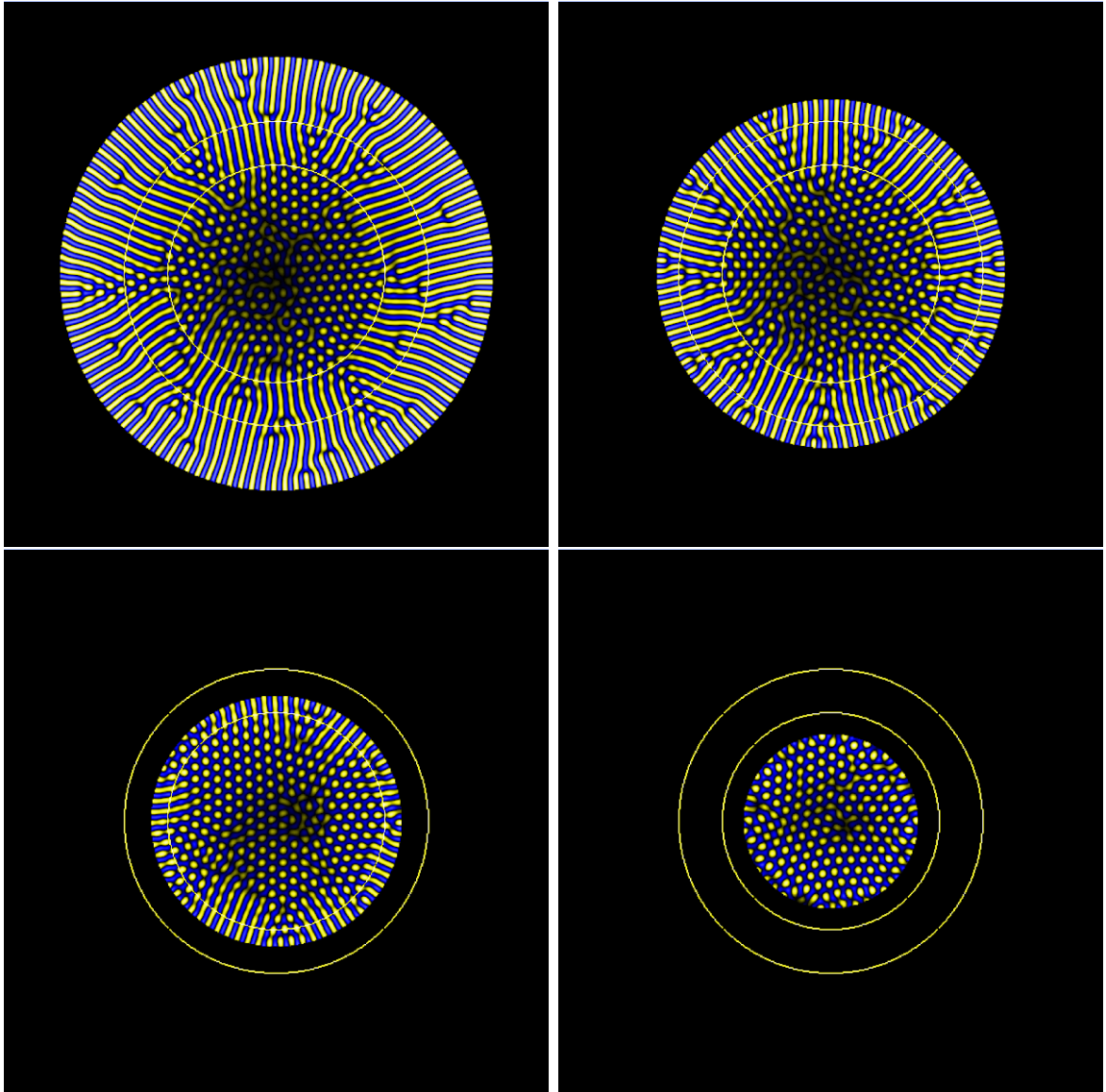


Figure 4.19: As Figure 4.18 except that the domain is now contracting, rather than expanding, with time. We see more or less the same sequence of events in reverse. In particular, the rolls disappear at (more or less) the same point at which they appeared, i.e. as the domain boundary passes through the innermost circle. In other words, there is little or no hysteresis between the point where the rolls appear in an ‘expanding’ run and where they disappear in a ‘contracting’ run.

pands (see Figure 4.19). Here we see more or less the same sequence of events in reverse, with the transition from ‘sunspot-like’ to ‘pore-like’ configurations again occurring as the boundary moves through the inner circle (corresponding to $\phi = \phi_{\text{pf}}$). In other words, the model shows no hysteresis between the two configurations as the domain is expanded and shrunk again.

Notice that the rolls in these images contain a number of dislocations along their length. We have already seen this phenomenon (e.g. Figure 4.16), and it can be explained as a way of maintaining the preferred wavelength of 2π despite the circular geometry. This pattern of rolls is seen in most of our runs, but we also find one other pattern in certain cases, and that is a spiral pattern; see Figure 4.20.

To obtain the spirals one must set the problem up quite carefully. In particular, they seem to arise only when the domain expands very slowly (and even then, only in some cases). Otherwise, the straight radial rolls will be seen. The spiral pattern is therefore an interesting quirk of the model, but may not be related to any particular phenomenon in sunspots.

Finally, note that there is a different time dependence between the two cases (Figures 4.18 and 4.20). In both cases, the hexagons travel inwards, but the behaviour of the rolls is different. In the former case (with straight radial rolls) the rolls are steady; in the latter case, the spiral pattern is observed to rotate with time. The spiral patterns can rotate because they break the rotational symmetry of the system. In addition, the pattern is drifting inwards at each point (for $c \neq 0$), which will create the impression that the entire pattern is rotating.

4.5 Conclusions

In this chapter we have constructed a modified Swift-Hohenberg equation that can be used to model convection in an inclined field where the inclination angle ϕ varies across the domain (in a predefined way). We have also derived a set of three coupled Landau-Ginzburg equations from this. This allowed the transition between rolls in one part of the domain and hexagons in another part to be investigated. The equations were studied in both Cartesian and circular domains – the former being easier to work with theoretically, and the latter being closer to a real sunspot.

The Cartesian results demonstrate two main points. The first is that there can indeed be a sharp transition, or front, between the hexagon and roll patterns (in the case where

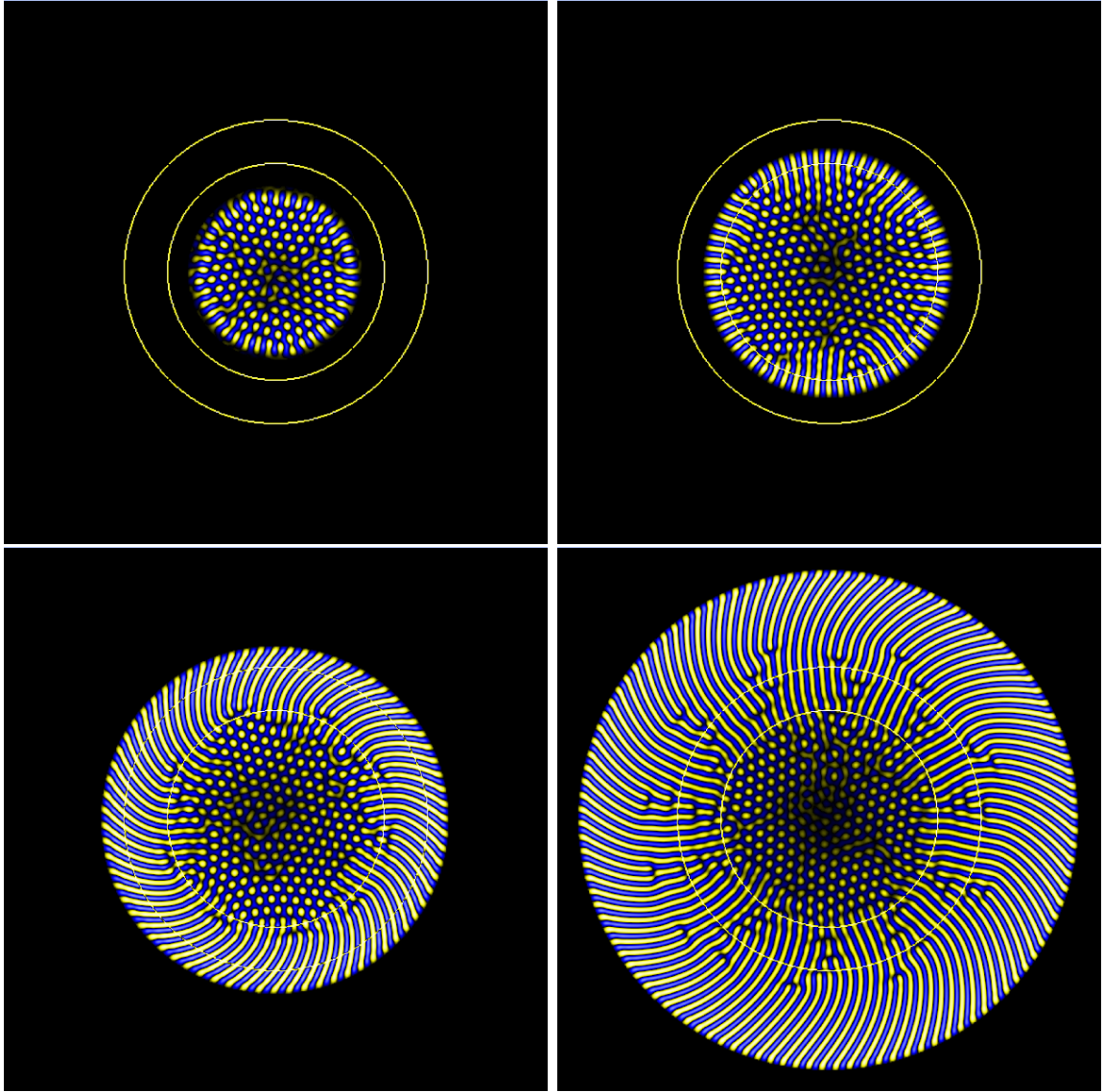


Figure 4.20: As Figure 4.18, except that here the domain has been expanded much more slowly than before (and also the Dirichlet boundary condition has been used). The rolls have formed a coherent spiral pattern, which appears to rotate with time (in a clockwise direction).

the bifurcation from hexagons to rolls is subcritical). The sharpness of the transition is limited only by the amount of diffusion in the system. The other effect demonstrated by the Cartesian results is that the hexagonal pattern travels, with a speed that depends on position; if ϕ decreases along the direction of travel, as in a sunspot umbra, then this causes the pattern to become compressed with time (since the ‘back’ of the pattern is moving faster than the ‘front’), eventually causing adjacent pairs of hexagons to be ‘squashed’ together.

More immediately applicable to sunspots are the results in the circular domains. Here, we find hexagonal convection in the centre of the domain, corresponding to the umbra of a sunspot, and rolls near the circumference, which would be the penumbra. The rolls are oriented radially, but because of the circular geometry, there cannot simply be a pattern of radial rolls without dislocations. Instead we find either a spiral pattern of curved rolls (which rotates with time, since the pattern is travelling inwards at each point), or, more commonly, a static pattern of straight radial rolls, with a number of dislocations.

These results are interesting because they show that certain features of sunspots can be understood using only a relatively simple model. In other words, whilst many sunspot phenomena undoubtedly require knowledge of the underlying solar physics for their explanation, there are nevertheless some aspects that can be understood in terms of simplified models using only minimal assumptions. Indeed, our model does not even use the MHD equations, relying instead on simple symmetry-based arguments, and yet it produces reasonably ‘sunspot-like’ results, if we interpret the hexagonal regions in our models as the ‘umbra’, and the regions containing rolls as the ‘penumbra’.

Among the features of real sunspots illustrated by the model is the fact that patterns tend to travel. Our model shows that the hexagonal patterns within the umbra tend to travel inwards; in real sunspots, travelling features are observed within both the umbra and the penumbra. This motion is naturally explained as a pattern drift, caused by symmetry breaking induced by the tilted magnetic field. Note that the direction of travel is not predictable from symmetry arguments alone – we know that patterns must travel, but we cannot say in which direction they will travel without knowing more about the underlying physics.

Another interesting feature of the model is that it shows quite clearly a transition in the pattern of convection from hexagons to rolls. This transition seems to be a fundamental property of magnetoconvection in inclined fields and its existence was

demonstrated in the weakly nonlinear models of the previous chapter. The results in this chapter illustrate how this can quite naturally lead to a two-component sunspot with both an umbra and a penumbra, if the magnetic field is sufficiently tilted at the edge of the spot. No special physics is needed; the transition occurs naturally as a result of the (minimal) assumptions built into the model.

As would be expected given the nature of the model, there are also many details of real sunspots that are *not* captured by our results. For example, the model only applies to weakly nonlinear convection; in the strongly nonlinear conditions found in the Sun, we would expect more complicated, and possibly more turbulent, versions of the hexagon and roll patterns to be present (although it seems likely that the transition from hexagonal to roll-like patterns would still exist in some form).

Another example is found in the penumbra: while our model ‘penumbrae’ consist only of simple radially-oriented convection rolls, real penumbrae have a more complicated structure, with distinct bright and dark filaments and an intricate interlocking-comb magnetic field configuration. Clearly, this magnetic fine structure requires a more complicated model for its explanation.

Indeed, our model does not allow for the possibility of azimuthal variations in the magnetic field inclination. Instead, the magnetic field configuration is specified in advance (by giving the vector $\phi(\mathbf{x})$) and is assumed to be unchanging during the calculation. In reality, we would expect the field to be rearranged by the convection. For example, Weiss et al. (2004) have suggested that the penumbral fine structure starts to form because of an instability leading to a fluted field configuration. If this is correct, then our model would represent a sort of ‘proto-sunspot’ configuration, at a stage before this instability has taken hold.

Another difference between our model and reality is that hysteresis between pores and sunspots is observed (the largest pores are larger than the smallest sunspots), but no similar effect is found in the model (see Figures 4.18 and 4.19). However, this is perhaps not surprising given that many important physical effects are not included in the model. For example, Weiss et al. (2004) suggest that flux pumping may be an essential part of the explanation. (See also Rucklidge et al. 1995 for a simple method of modelling this hysteresis.)

In summary, we see that the model presented in this chapter, a model based on simplified equations and including very little in the way of solar physics, can nevertheless produce results that are reasonably sunspot-like. It illustrates how some of the basic

properties of sunspots can be explained using only simple symmetry-related arguments – for example, a transition between umbra and penumbra seems almost inevitable, given the transition from hexagon-like convection to roll-like convection that must occur as the field becomes more tilted. Of course there remain many details that the model gets wrong, and that require more intricate explanations, based on detailed solar physics models: for example, the direction of travel of umbral and penumbral features (either inwards or outwards), or the complex fine-scale structure of the penumbra. These can ultimately only be explained by performing three-dimensional numerical simulations, and this is the subject that we will turn to in the next chapter.